

Scattered Emission from W49N OH Maser Sources

Mendoza-Torres J.E. ¹, Goss W.M. ², Streb S. ³, Deshpande A.A. ⁴,
Laskar T. ^{5,6}

¹ Instituto Nacional de Astrofísica, Óptica y Electrónica, Apartado Postal 51 y 216, Puebla, Pue., Z.P. 72000, México

² NRAO

³ Salpointe Catholic High School, Tucson, AZ

⁴ Raman Research Institute, Bangalore, India

⁵ Department of Physics, Cavendish Laboratory, University of Cambridge, JJ Thomson Avenue, Cambridge CB3 0HE, UK

⁶ Space Telescope Science Institute, 3700 San Martin Dr., Baltimore, MD 21218, USA

Received ...

Abstract. We have analyzed VLBA observations of W49N at the OH maser frequencies 1612 MHz, 1665 MHz and 1667 MHz. More than two hundred masers spots were detected. For all of them the Major axis, the minor axis, the principal axis (PA), the central velocity and the linewidth were measured. The deconvolved angular size of the major axis range from 30 to 70 mas, the minor axis from 20 to 50 and the PA takes values from 70° to 130° . At the same field of the observed OH masers there are seven UC HII regions. Some of OH maser spots are cospatial to UC HII regions but many other are not. Other spots are in zones with no HII regions. It is found that subsets of OH spots are forming structures, among them a small and a large arc, a jet and a ring. The magnetic field at the OH sources is estimated based on Zeeman pairs. The magnetic fields at the small arc, at the jet and at the ring show a regular behaviour with smooth variations but at the large arc the field varies aleatory. Although the OH spots are spread over a wide field and located at very different structures their PA s have similar values to each other. The fact that the PA of distant spots are oriented at similar directions indicates that they could be due the result of scattering by density inhomogeneities elongated along an ordered component of the galactic magnetic field. Histograms of the spots parameters and plots to search for correlations were made. At 1665 MHz and 1667 MHz the Major axis, the minor axis, and the PA

show a different behavior with frequency and polarization. This result seems to be due to scattering of radio waves by density inhomogeneities elongated along an ordered component of the galactic magnetic field. We estimate whether the values could be explained in the frame of a structure function for a power law spectrum of density inhomogeneities of the interstellar plasma. It is found that two different inner length scales of the power spectrum, along and perpendicular to the magnetic field, could explain some of the observed differences.

Key words. Masers: OH, Masers: Zeeman

1. Introduction

W49N is a Star-Forming-Region (SFR) located at a distance of 11.4 kpc (Gwinn et al. 1992) at a low galactic latitude, close to the disc. It is characterized by the presence of a number of HII regions (Dreher et al. (1984) and De Pree et al. (2000)) and, in a smaller scale, by H₂O maser spots tracing two oppositely directed outflows. The HII regions, initially identified by Dreher et al. (1984) as ultracompact (UC) and now referred to as hyper-compact (HC) H II regions (Kurtz 2000) because are about one order of magnitude smaller than UC HII regions (Kurtz & Franco 2002), are thought to be driven by O stars, making this region one of the sites at our Galaxy with active formation of massive stars.

Since the HC H II regions are typically about two orders of magnitude denser than UC HII regions, the W49N region seems to have conditions (De Pree et al. 2000) where the HII regions reach the equilibrium with the environment at shorter distances than typical UC HII regions (Wood & Churchwell 1989). OH masers have been detected at W49N. The presence of O stars create an ideal scenario to switch-on OH maser emission thus making it a source rich in OH maser spots that could give an insight into the environment of the HC HII regions. Also, estimates of the magnetic field have been done for OH maser sources (Fish et al. 2006). Such estimates are clue to have an idea of the role that magnetic fields could play in such particular regions.

The density inhomogeneities of the interstellar medium efficiently scatter emission at frequencies below ≤ 10 GHz (Rickett, 1990). Pulsars have been widely used to estimate the spectrum of these inhomogeneities (Gwinn et al. 1993 and literature therein). Observations towards HII regions (Moran et al. 1990) where dense plasma could considerably increase scattering of radio waves also have been used. The apparent sizes of OH maser spots have been interpreted as the result of electron density inhomogeneities (Diamond et al. 1988). The sizes of 1665 MHz OH maser spots have been observed to increase with distance due to scattering, reaching apparent sizes of about 50 mas at 10 kpc

(Diamond et al., 1988). Also, it has been noted that the scatter increases as approaching to galactic disk latitudes (Cordes et al., 1984).

We may see, from the above discussion, that the OH maser emission from W49N, at a distance of 11.4 kpc, it is expected to be heavily scattered due to the contribution of electron density inhomogeneities close to the maser source and at intermediate locations in the rays path from the source to the Earth.

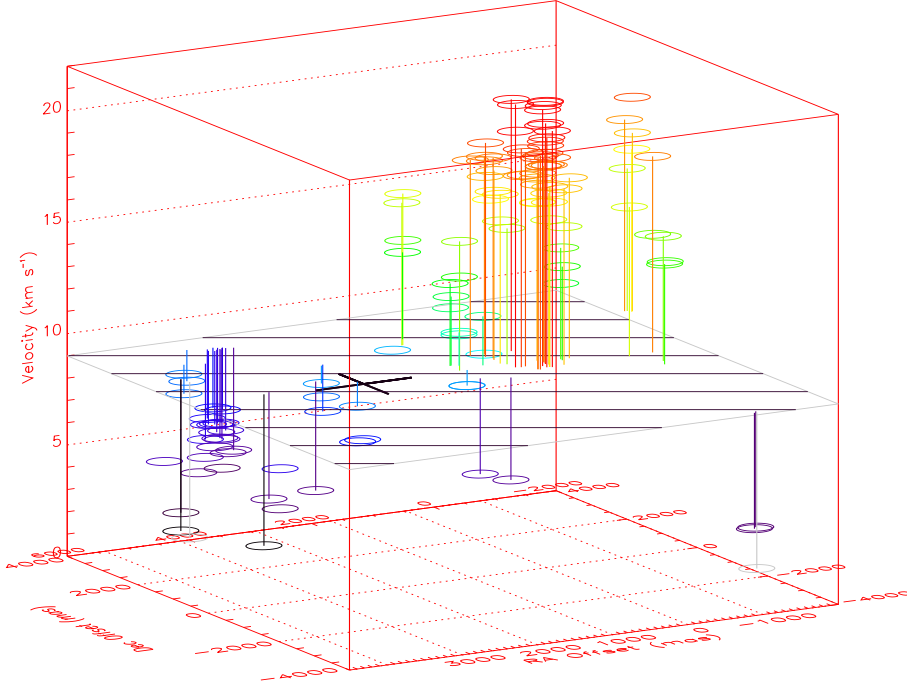


Fig. 1. 3D scatter plot for the spots at 1667 MHz, a plane at a velocity of 9 km s^{-1} , which is around the central velocity, is plotted as reference. The color of each ellipse is proportional to its velocity, purple is for blue-shifted and red for red-shifted.

2. Observations and data analysis

The 1667.35903 MHz (hereafter 1667 MHz), 1665.4018 MHz (hereafter 1665 MHz) and 1612.23101 MHz (hereafter 1612 MHz) transitions were observed toward W49N with the VLBA on 2005 October 6.

The reference coordinates are RA=19 10 13.2091 and Dec=09 06 12.485. Left Circular Polarization (LCP) and Right Circular Polarization (RCP) are observed simultaneously in about 240 spectral channels with a resolution of 0.1 km s^{-1} in a range of about 22 km s^{-1} . The beam size is about 20 mas by 15 mas at a position angle of 84 degrees. The galactic plane is at a position angle of 30° .

We have detected 208 spots and all have an elliptical shape whose major axis (further denoted when necessary as M), minor axis (also further denoted when necessary as m) and the Principal Angle (PA) are estimated using the JMFIT AIPS routine (Tables 6-

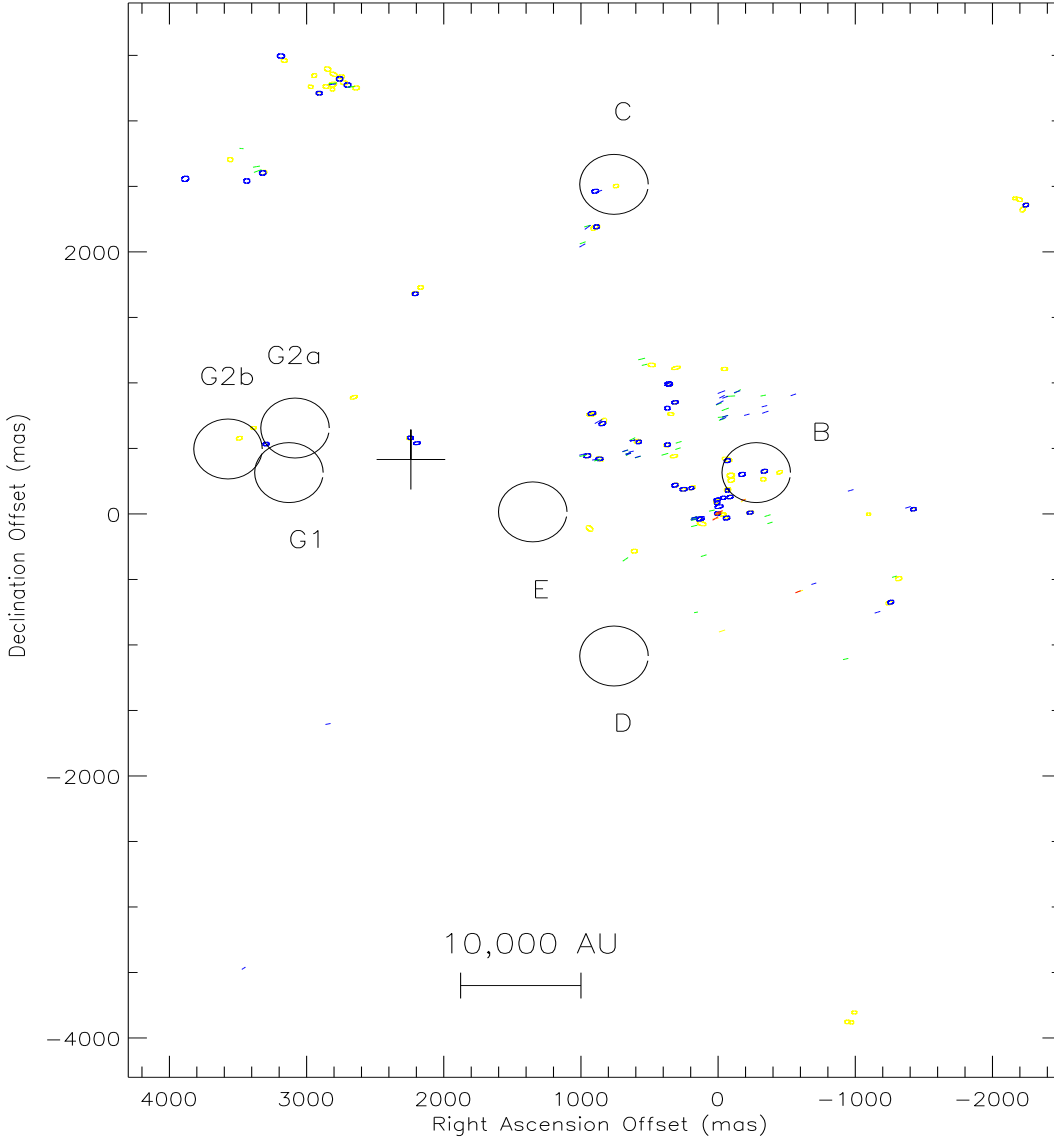


Fig. 2. Distribution of W49N spots. Yellow ellipses are for LCP 1667 MHz spots, blue ellipses for RCP 1667 MHz spots. The ellipses are of the actual sizes and are oriented at the PA observed in each case. The extension and orientation of the bars denote, respectively, the Major axis and the PA of the spots as follows, LCP 1665 MHz (green bars), RCP 1665 MHz (blue bars), LCP 1612 MHz (yellow bars), RCP 1612 MHz (red bars). The circles denote the HII regions C , E , B and G of Dreher et al. (1984) and $G1$ and $G2$ of De Pree et al. (2000). The CE of Gwinn et al. (1992) is denoted by a *cross*.

11). The XGAUSS routine was used to estimate the center and width of the spectral line for each spot as given at the same Tables.

Histograms for the parameters of the 1665 MHz and 1667 MHz spots, are made (Figs. 6, 7, 8, 9 and 11). Gaussian functions are fitted to the histograms to have an estimate of the mean values and of the spread of the distributions (given by the width of the Gaussian at e^{-1} , which further is referred to as σ). The mean values of the Gaussians are used to estimate turbulence parameters. It should be noted that the distributions

for the width of the lines are not well fitted by Gaussians but the mean values of these distributions are not used in the estimations. Also, scatter plots for the different spots parameters against each other are made to look for possible correlations.

3. Spatial distribution of spots

A total of 208 spots were detected. At the three frequencies more spots at LCP than at RCP were detected (Table 1). The major axis of the spots takes values between 30 and 70 mas, which for a distance of 11.4 kpc corresponds to 350 and 800 AU.

Table 1. Amounts of detected spots

ν	L	R	L+R
1667	76	44	120
1665	42	35	77
1612	6	5	11

The OH spots are distributed on a field of about 6 " (Fig.1), that corresponds to $7 \cdot 10^4$ AU. Two main groups are seen nearly aligned in North-East to South-West direction (Fig.2). OH spots have been previously observed with a larger uncertainty but at the same field that the spots reported here (Kent and Mutel, 1982). H₂O spots have been observed in a more compact distribution that is lengthen in East-West direction (Gwinn et al, 1992) and that traces flows from a Center of Expansion (CE) (denoted by a *cross* in Fig.1 and Fig.2). Eastern H₂O spots are slightly to the north respect the Western ones.

The velocities of the OH spots that lie near the CE on the West side have velocities ≤ 9 km s⁻¹ and the spots near CE on the East side have velocities ≥ 9 km s⁻¹. Coincidentally, the middle of the range of velocities of the spots becomes about 9 km s⁻¹. In Fig.1 a plane is plotted at this velocity. It may be seen that most of the spots with blue velocities, respect 9 km s⁻¹, are located at the West, while red shifted spots predominantly appear at the East. This behaviour is similar to that observed by Kent and Mutel (1982) also for OH spots. However, the H₂O spots show a distinct behavior; the East H₂O spots are red shifted and the West are blue shifted. It means, the H₂O velocities are of the opposite sign respect the OH ones. The interpretation of this result is not straightforward but could due to large inflows that influence the OH spots velocities and outflows at the shorter scale of the H₂O spots.

In Fig. 2 the locations of the observed maser spots are denoted by small ellipses and small bars, the locations of HII regions observed by Dreher et al. (1984) and De Pree et al. (2000) are denoted by circles.

4. Spots forming structures

It has been found that some groups of spots seem to trace some particular structures.

4.1. Small arc

A subset of six spots (three at LCP and three at RCP 1667 MHz) form a small arc. The yellow ellipses denote the LCP and blue the RCP 1667 MHz spots. The bars are for 1665 MHz (green for LCP and blue for RCP) and 1612 MHz spots (yellow for LCP and red for RCP). A circle is fitted to the spots (small dashed circle of Fig.3) and the cross on the East corresponds to the center of the circle. The six spots form Zeeman pairs. The estimated magnetic fields are given in Table 14. A velocity gradient takes place from East to West, it may be seen in Fig. 5 where the distance is referenced to the Eastern spot.

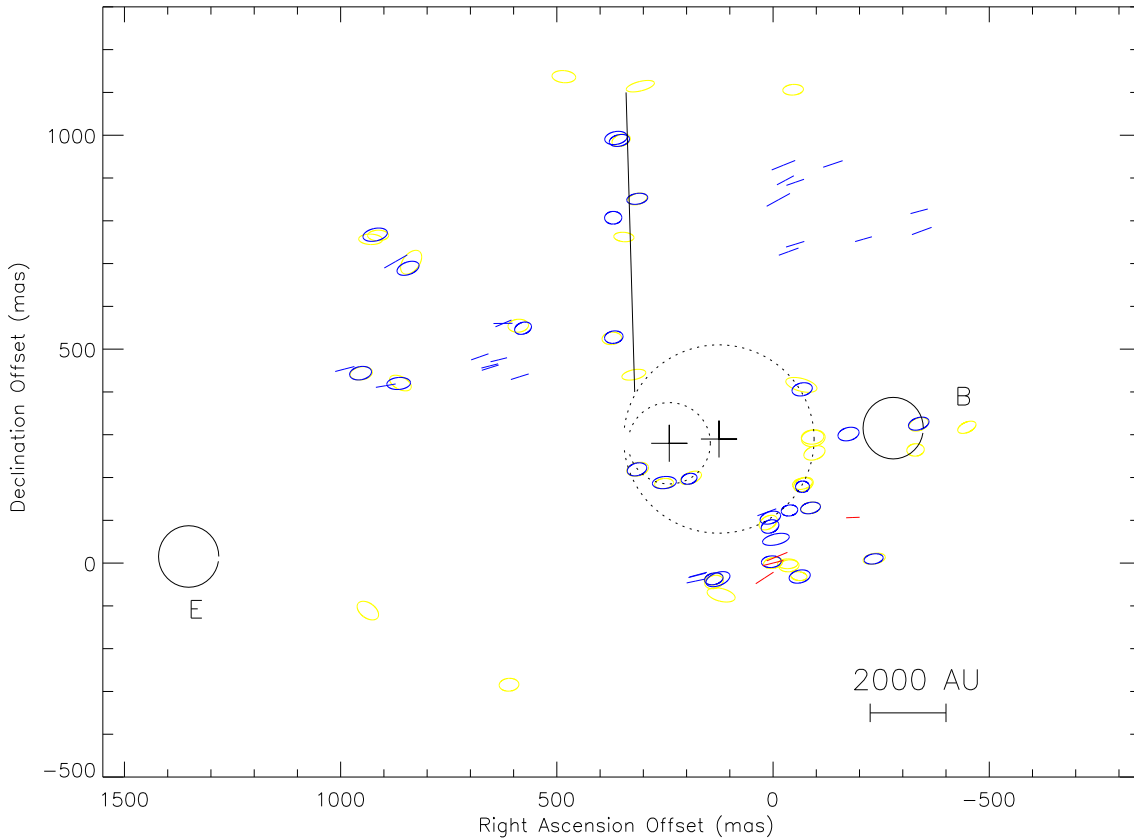


Fig. 3. A subset of spots at the Western side (right hand side) of Fig.2. Yellow ellipses are for LCP 1667 MHz spots, blue ellipses for RCP 1667 MHz spots. The ellipses are oriented at the PA observed in each case, and their sizes are the actual ones. The extension and orientation of the bars are as in Fig.2. The dashed circles indicate arcs formed by spots. The velocity of the spots that lie at the large circle increases clockwise, i.e. from North (16.1 km s^{-1} LCP 1667 MHz) to South (20.7 km s^{-1} LCP 1667 MHz). Also the velocity of the spots at the small arc grows clockwise, from West (18.6 km s^{-1} LCP 1667 MHz) to East (20.8 km s^{-1} LCP 1667 MHz).

4.2. *Large arc*

A subset of spots forms an arc of about 0.5 sec length. At the West and at the South-West of the arc some spots are located in a sequence to the West and to the South-West as if they would be in a filament. The distribution of these spots (including those outside the drawn field) are roughly aligned as going away from the gaps in the arc Fig.2.

The northern half of the arc seems to trace a velocity gradient going from 16.1 km^{-1} at the North to 20.7 km^{-1} at the South. The large dashed circle of Fig.3 fits well to the spots at the north part of the large arc. The center of this circle is at the West of the center of the small dashed circle.

4.3. *Jet*

A subset of 1665 and 1667 MHz spots is roughly distributed following a straight line, as that plotted in Fig.3. The jet has a length of 700 mas ($\sim 8000 \text{ AU}$). The velocity of the LCP 1667 MHz spots goes from about 15.2 km s^{-1} at the South to 18.7 km s^{-1} (at 550 mas North $\sim 6300 \text{ AU}$) where the velocity has a turnover to smaller values. The behaviour of the velocity along these spots indicates that they are located in a jet. The velocity of the RCP spots is smaller relative the LCP one. This is due to the presence of magnetic fields (Fish et al. 2006) and will be below discussed.

4.4. *Ring*

Another subset of 1667 MHz spots forms a ring whose diameter is about 800 AU. Each spot at the ring appears at several channels. The location of some spots differs from one channel to other. The *PA* of the five Eastern spots of the ring has a tendency to be tangent to the ring but at the same time does not considerably differs from the orientation of the other spots at the field. In general, the positions of the maser spots change from one channel to other. In a subset of the spots at the West side the shift is considerably larger than in the other spots. The positions go from the inner side to the outer side of the ring, roughly located in East-West direction, with an extension projected on the sky, similar to the ring diameter. These spots are the more intense at the ring. HII regions with a ring shape have been observed at W49N (De Pree et al., 2000). One of them is at the North, out of the field of view of the present plot. Hollenbach et al. (1994) suggest that such UC HII regions may result of photoevaporating circumstellar disks.

5. Estimation of the magnetic field by using Zeeman pairs

The Magnetic field along the line of sight is estimated at locations where two spots of opposite polarization spatially coincide. The errors in the estimations of the spots

coordinates are used to determine whether the offset in the coordinates is significant or not. To estimate the magnetic field (B) the next equation is used,

$$B = \frac{\Delta v}{C} \quad (1)$$

where Δv is the difference between the velocities and C is a constant that depends on the frequency. The constant is given in $km\ s^{-1}/mG$ and it is 0.122 for 1612 MHz, 0.590 for 1665 MHz and 0.354 for 1667 MHz. The error in estimating the central velocity of a spot with the XGAUSS routine typically is less than $0.01\ km\ s^{-1}$. The largest errors are $\leq 0.03\ km\ s^{-1}$. Therefore, the error in the estimation of the magnetic field is $\leq 0.25\ mG$ for 1612 MHz, $\leq 0.05\ mG$ for 1665 MHz and $\leq 0.08\ mG$ for 1667 MHz. In Table 12 the Zeeman pairs are given. Taking into account the small errors in the estimation of the central velocity, we give the velocities in Tables 12, 13 and 14 with two decimals. The computation of the magnetic field was done based on the velocity difference between such values. We found that, in some cases, the shift in locations is larger than the errors because the orientations of the PA are considerably different. That cases are also listed in Tables 13 and 14 as Zeeman pairs.

5.1. Magnetic field at the small arc

In Fig.5 **a**) the velocity of the LCP (open circles) and RCP (closed circles) 1667 MHz spots located at the small arc are given versus distances. The distances are referenced to the Eastern spot. The difference in velocity between LCP and RCP velocities is due to the local magnetic field (Fish et al. 2006). The six spots form Zeeman pairs whose estimated magnetic field is given at the corresponding pair between the velocities of LCP and RCP spots at the distance of the spots, respect the reference. The magnetic field is nearly constant for the arc with an indication of a smooth gradient (of $\sim 3.3 \times 10^{-4}$ mG/AU) with decreasing strength from East to West.

5.2. Magnetic field at the jet

In Fig.5 **b**) the velocity and distance for the spots located at the jet are shown. Also, the open circles are for LCP and closed circles for RCP 1667 MHz data and the estimated magnetic field is shown between the data of the corresponding pair. Three pairs are found at the jet. It may be seen that the LCP spots at distances from 100 mas to 550 mas may be fitted by a straight line. The RCP spots from 0 mas to 550 mas also may be fitted by a straight line. The velocity difference between the lines fitted is nearly constant with a small increase (in a spatial scale of $\sim 700\ mas$ ($\sim 8000\ AU$)). In spite of the fact that not all the spots fitted by these lines are Zeeman pairs one may consider that the behavior of the magnetic field accomplish also for the intermediate locations (as if there were spots forming pairs along the straight lines). It is interesting to note that the difference

5

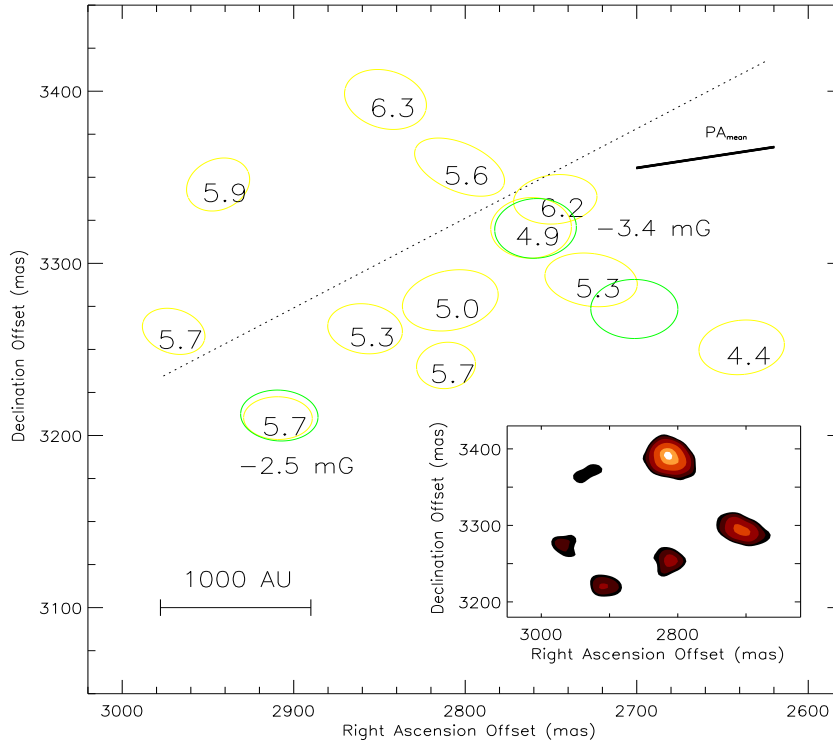


Fig. 4. In the main panel the yellow ellipses denote the LCP spots and the green ellipses the RCP spots observed at 1667 MHz forming a ring at the North-East of the field. Ellipses are of the actual sizes. The orientation and the sizes are as estimated by the JMFIT routine. The dotted line indicates a constant Longitude. The values inside yellow ellipses are the velocities. The values at a side of a spot pair (coincident yellow and blue ellipses) are the estimated magnetic fields. The bar on the right-lower corner indicates the orientation of PA_{mean} , the mean value for the 1667 MHz spots (Fig. 8). The three northern spots attained the maximum flux at other velocities. The location, the orientation of PA and the Major axis of the bars for these spots correspond to the values at the velocity of maximum flux of each of them. It may be seen that the orientations of the spots with velocities 5.6 km s^{-1} and 5.7 km s^{-1} (at the East) considerably differ from that of constant galactic longitude and from PA_{mean} . In the subframe the LCP spots at 5.7 km s^{-1} observed at 1667 MHz are plotted. Not all the spots attained the maximum flux at this velocity.

between LCP and RCP velocities decreases at the locations where the maximum velocity is reached. This smaller difference means a weaker magnetic field in this region. According to Fig. 3 further to this point the spots spread by $\sim 200 \text{ mas}$ ($\sim 2300 \text{ AU}$). At the reference location there are no RCP spots. However, if we extrapolate the RCP line to the initial location the RCP velocity comes to the same value as the observed LCP velocity, which would correspond to a zero magnetic field at the southernmost location of these set of spots. From 100 mas to 350 mas there is an increasing magnetic field but at the distance of 350 the field decreases. The increasing magnetic field would accelerate charged particles

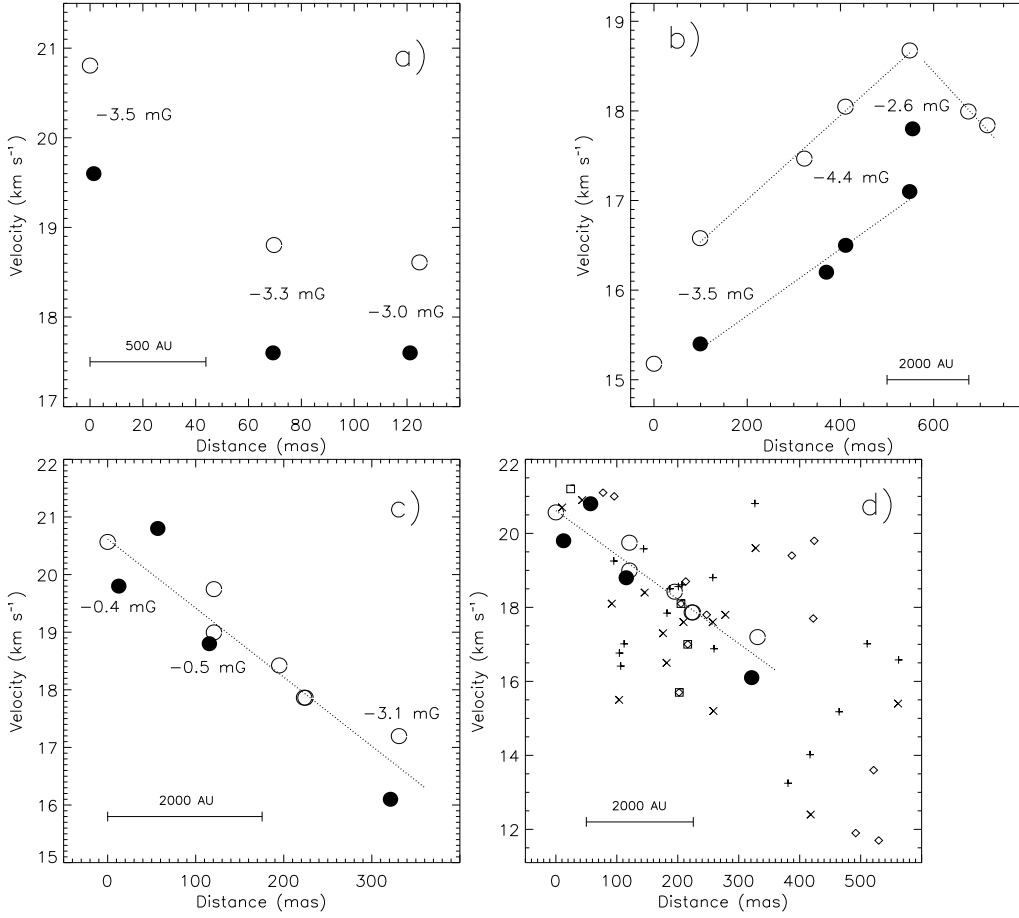


Fig. 5. The velocity as a function of the distance of the spots (open circles denote LCP 1667 MHz data and closed circles RCP 1667 MHz data) at, **a)** the small arc. The distance was measured taking as reference the location of the Easternmost spot. The values given between pairs of LCP and RCP data correspond to the estimated magnetic fields. **b)** the jet (denoted by the vertical straight line of Fig.3), **c)** the large arc, taking into account only the spots that lie at the large circle drawn in Fig.3. **d)** the large arc and the spots with values at the velocity and distance ranges of this plot. The *plus* denote the LCP 1667 MHz data of spots that do not lie at the arc but are at the distances in the range of this plot, the *product* denotes the RCP 1667 MHz data, *rombes* the LCP 1665 MHz data and *squares* the RCP 1665 MHz data .

while the decreasing magnetic field would brake down charged particles. This magnetic field could be the origin of the accelerated stream of particles along the jet.

5.3. Magnetic field at the large arc

In Fig.5 **c)** the velocity and distance for the spots at the large arc are plotted. Distances are given respect the southernmost spot. The open circles denote LCP and closed circles the RCP 1667 MHz data. Distances are measured taking as reference the spot at the South-East of the arc (of those that lie at the large dashed circle). The straight line is fitted for LCP and RCP data together. It may be seen that about the location of the

reference spot and at a distance of 300 mas (~ 3800 AU) the LCP velocity is smaller than RCP one. However, there are no clear trends for the velocity variations neither for LCP nor for RCP data and there is no a tendency of the velocity difference to be around a given value or have regular variations. Around the region of the spots with magnetic field of -0.5 mG, at a distance of 100 mas (~ 1100 AU) there is a Zeeman pair for which the estimated magnetic field is -3.7 mG. At other locations of the backside of the large arc there are some other Zeeman pairs that lead to magnetic fields that differ from those at the arc by few milliGauss. These values and the values at the arc itself, indicate that the magnetic field at the arc and at its back side have large differences even between near locations. This behaviour considerably differs from that of the magnetic field at the small arc and at the jet. In Fig.5 **d**) the data of spots of Fig. 3 is plotted together with those at the region that are not farther than 600 mas (~ 7000 AU) from the reference spot. It is clear that in this set of spots also is seen a velocity decrease as the distance increases. This could indicate that the spots near to the arc are dynamically related to the arc and to the source that drives it.

5.4. Magnetic field at the ring

A Zeeman pair is observed at the NW of the ring. It leads to a magnetic field estimation of -3.4 milliGauss. At the South of the ring another pair leads to a field of -2.5 milliGauss. The behaviour of the magnetic field at the ring can not be estimated base on these two pairs. However, the fact that the locations of the spots change from one channel to other is indicative of the presence of a magnetic field all around the ring. Since the *LCP* 1667 MHz spots are weak then *RCP* 1667 MHz emission probably is even more weak to be detected.

6. Spatial distribution on galactic Coordinates

The distribution of the spots galactic coordinates are shown in Fig.6 and Fig.7. It may be seen that the behaviour differs from each other. The distribution of the Longitudes does not follow a single Gaussian shape neither for a histogram with binning interval of 200 mas (Fig.6) nor for a 500 mas one. Moreover, there are gaps that separate groups of more than ten spots. One of these groups has more that twenty spots. It is as if the groups were clumped at different longitudes. The 1612 MHz spots lie at smaller longitudes than 1665 MHz and 1667 MHz spots. Clearly, the 1612 MHz spots are at Longitudes at an extreme of the 1665 MHz and 1667 MHz distributions. On the other hand, the Galactic Latitude for the spots at the three frequencies are clumped around a mean value of about 42.5 (Fig.7). At the histogram made with a binning interval of 200 mas there are no important gaps (the separated groups has less than ten spots). In the histogram made

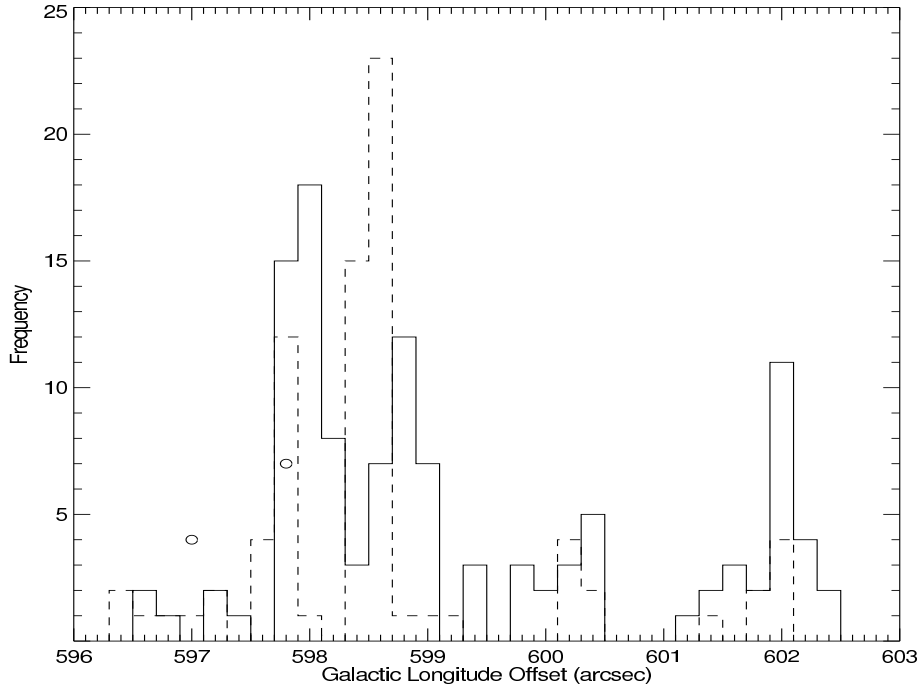


Fig. 6. Number distribution (histogram) of the Galactic Longitude for the 1667 MHz spots (continuous line), for the 1665 MHz spots (dashed line) and for the 1612 MHz spots (circles). The Longitude Offset is given respect the galactic center.

with a binning interval of 300 mas one of these gaps disappears and the remaining groups have five or less spots.

7. Spots parameters

7.1. Principal axis orientation (*PA*)

For the three frequencies and both polarizations the principal axis (*PA*) takes values from about 70° to 130° , i.e., even though the spots are spread more than 6sec ($7 \cdot 10^4$ AU), their *PA*s are all nearly aligned. In Fig. 8 the histograms of the *PA* of the 1665 MHz and 1667 MHz spots are shown. Gaussians fitted to each histogram are also plotted (continuous for 1667 MHz and dashed for 1665 MHz). It may be seen that the mean of the 1665 MHz spots histogram clearly becomes at a larger value than the 1667 MHz one and has a smaller data dispersion (measured with the σ of the fitted Gaussian). At LCP (and RCP) data occurs the same situation, i.e. the mean of the distribution of LCP (RCP) 1665 MHz *PA* data becomes at a larger value than the LCP (RCP) 1667 MHz *PA* data, and is less dispersed. It means, both polarizations contribute to the difference between the behaviour of the histograms of the two frequencies.

The fact that the mean *PA* for 1665 MHz (106.3°) is closer to the galactic plane and has a smaller dispersion than the mean *PA* for 1667 MHz, (98.6°) indicates that the observed orientation of the spots is a function of the wavelength. Between the histograms of LCP and RCP there are differences at each of the polarizations. The RCP histogram of

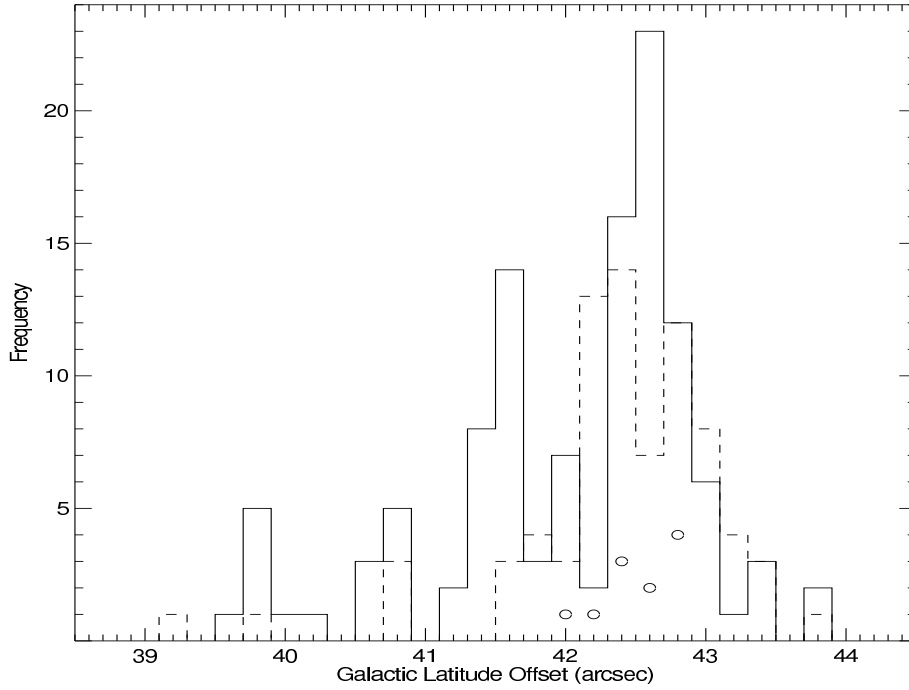


Fig. 7. Histogram of the Galactic Latitude for the 1667 MHz spots (continuous line), for the 1665 MHz spots (dashed line) and for the 1612 MHz spots (circles).

the 1667 MHz PA data is centered at a larger value than the LCP 1667 MHz PA data, and is less dispersed. On the other hand, for 1665 MHz spots the mean and dispersion values are similar for LCP and RCP 1665 PA data.

As may be seen from Fig.13, the behaviour of PA with the peak of the spot (maximum flux) is straightforward. PA converges to a value near 107° (which is near to the angle perpendicular to the galactic plane) as the flux of the spots increases. This indicates that as intense the emission as closer the spot Orientation will be to the angle perpendicular to the magnetic field. This also implies that there is a limit to the PA orientation.

7.2. PA at the structures

We have found that some extreme PA values take place for spots in well defined structures such as a ring and an arc. As an example, we may see that the PA of the five Eastern spots of the ring has a tendency to be tangential to the ring with differences between the PAs at the ring of about 50° . However, the PAs are not fully tangential to the ring, i.e. at the same time the PAs retain the orientation that makes them not to considerably differs from the orientation of the other spots at the field. It means, the location on the ring does not fully determines the orientation. The distance between spots of the W49N OH field is several times larger than the distance of opposite spots at the ring and nevertheless many of them are oriented at the same angle. Also, it may be seen that the PA of two LCP 1667 MHz spots (yellow ellipses of Fig. 3) located at both extremes of the large arc considerably differ from the mean value but are similar to each other.

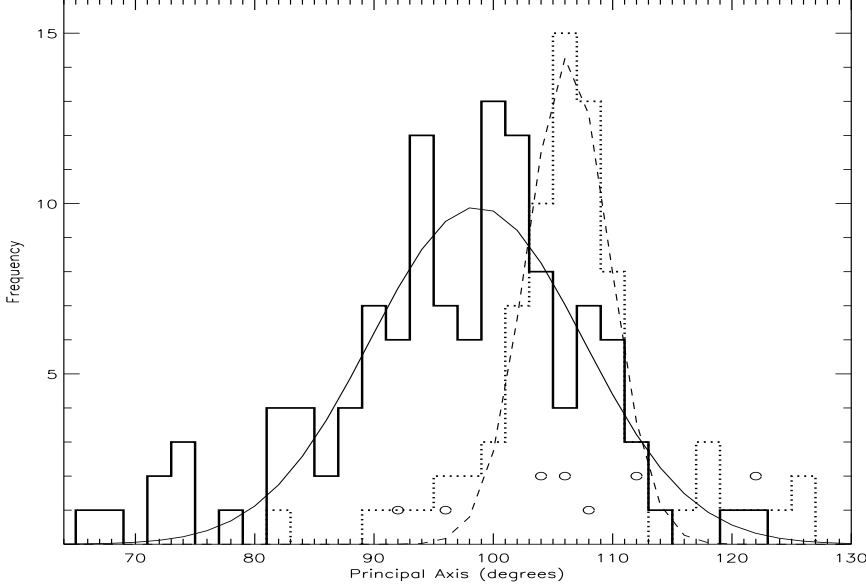


Fig. 8. Histograms of the angle of orientation of the Principal Axis (PA) of the 1667 MHz spots (continuous line), of the 1665 MHz spots (dotted line) and of the 1612 MHz spots (circles). A thin continuous line denotes a Gaussian fitted to the 1667 MHz histogram and a dashed line a Gaussian fitted to the 1665 MHz one. The mean values of the fitted Gaussians are 98.6° and 106.2° for LCP 1665 MHz and RCP 1665 MHz, respectively.

The above results indicate that PA depends on both the local magnetic field and the global magnetic field. Then, we cannot attribute the spread of the spots PA to the distance between them but to the difference between the local magnetic fields that influence the orientation at structures such as the above mentioned ring and that makes them to differ from the other spots at the observed field.

7.3. Major and minor axes

In Fig.9 the histograms of the Major axis data for 1665 MHz and 1667 MHz are shown. To estimate the width of the distribution for major and minor axes, we have also fitted a Gaussian to each histogram.

The histogram for the Major Axis of the 1667 MHz spots is centered at a larger value than the 1665 MHz one (Fig.9). The σ for the Major Axis of the 1667 MHz spots is about twice the σ for the 1665 MHz spots. This happens also for the histograms of LCP and RCP Major axis data. For the Minor Axis also the centers become at different values but the differences are smaller. However, there is a clear difference in the σ . A particular feature is a large spread of the Minor Axis of LCP spots (both 1665 MHz and 1667 MHz) relative the spread of RCP spots.

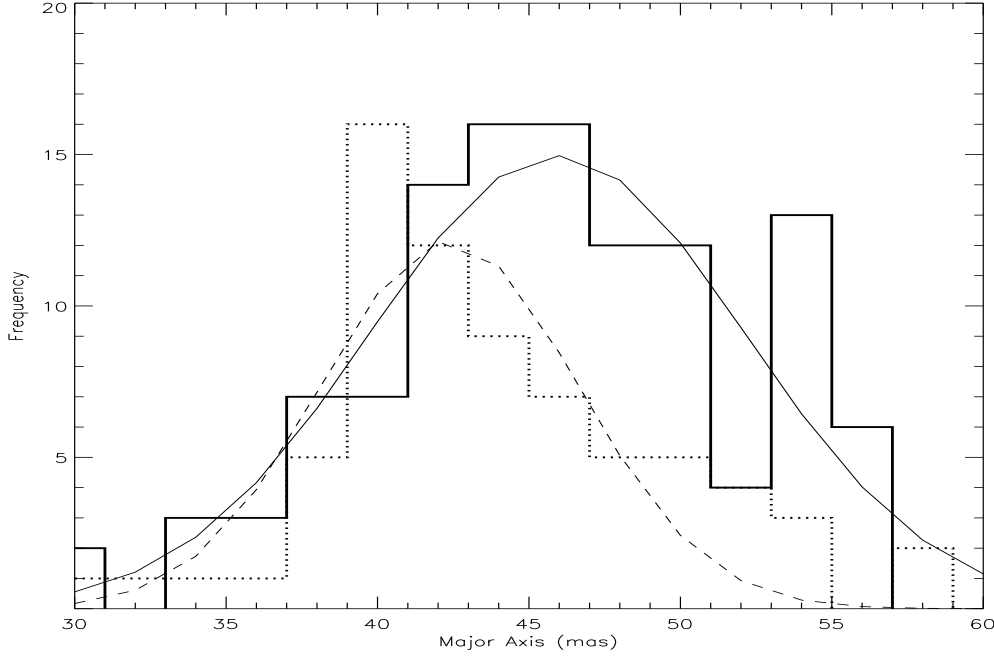


Fig. 9. Histograms of the Major Axis of the 1667 MHz spots (continuous line) and of the 1665 MHz spots (dotted line). The fitted Gaussians are as in Fig.8 The 1667 MHz fitted Gaussian is centered at 45.9 mas and the 1665 MHz one at 42.4 mas (Table3).

7.4. Linewidth

Histograms for the widths of the spectral lines of the spots were made. There are no clear differences between the spots of the different frequencies but the values for the few 1612 MHz spots tend to be larger. However, in the histograms made for spots whose maximum flux is larger than 1Jy/beam the mean value of the width increases with the wavelength. It means, the mean width for 1667 MHz is smaller than the 1665 MHz mean and this is smaller than the 1612 MHz one.

The central wavelength of a spot depends on the local conditions at the masing region. On the other hand, the width has the influence of the medium between the source and the observer. In fact one could expect that the stronger the scattering the wider the line. Excluding the correlation between the maximum flux and the width no correlation was found between the width and other spot parameter.

8. Correlations between spots parameters

8.1. Relation between Major and minor axes

In Fig.10 the Major axis values are plotted versus the minor axis ones. It may be seen that, for the three frequencies, the axes ratios fall between 1:1 and 1:3 but the bulk of them fall in a short range around a value slightly larger than 1:1.5.

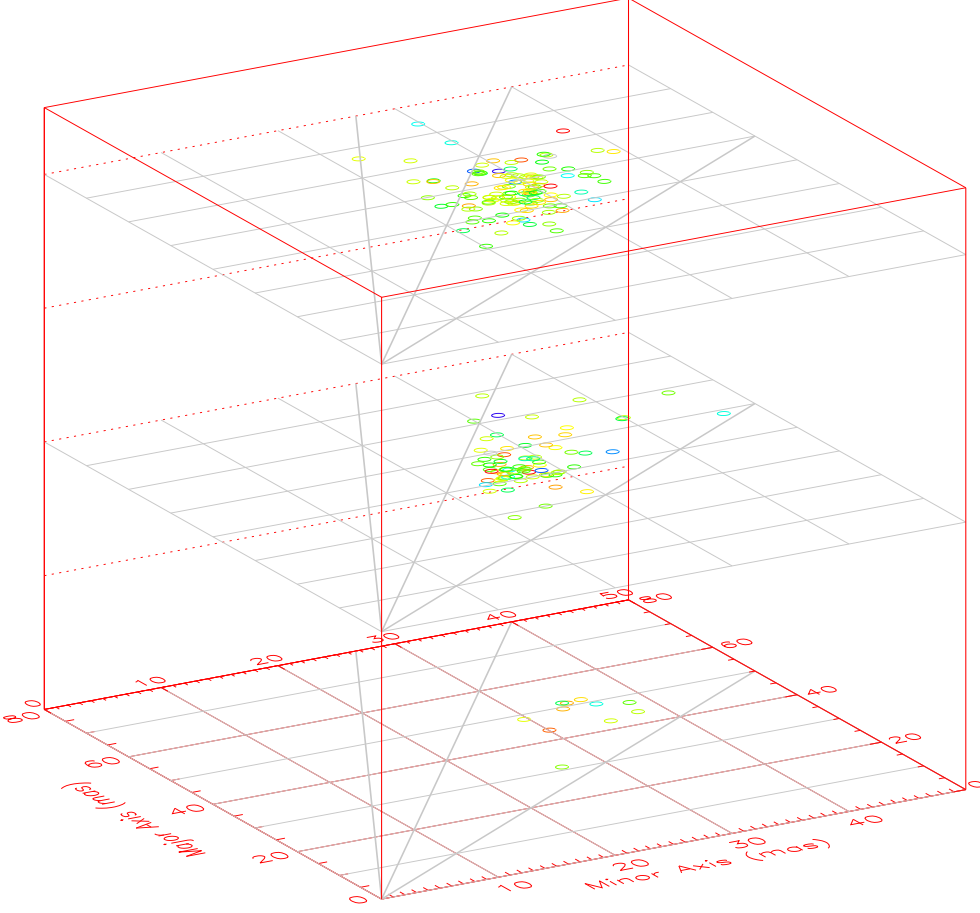


Fig. 10. Scatter plot of the Major Axis versus the Minor Axis. The lower plane corresponds to the 1612 MHz, LCP and RCP data, the middle plane to the 1665 MHz, LCP and RCP data and the upper to the 1667 MHz, LCP and RCP data. The straight inclined lines on each plane indicate the 1:1 (lower), 2:1 (middle) and 3:1 (upper) ratios. The colors correspond to the PA values, going to red for large values (about 130°) and to purple for low values (about 70°).

We computed the M/m ratio for each spot and estimated the mean value for the ratios at the different frequencies and for the different polarizations. Probably, the above mentioned short range leads to shapes of the distributions of the M/m ratios for the 1665 MHz and 1667 MHz spots that are similar to each other. In Fig. 11 the histograms of the M/m ratio of 1665 MHz spots and the histogram of the 1667 MHz spots are plotted. The mean and σ values of the Gaussians fitted are very similar to each other. On the other hand, we found that the histogram of the $M \cdot m$ product leads to distributions where the mean values considerably differ to each other. The $M \cdot m$ product increases the differences between the centers of 1665 MHz and 1667 MHz histograms found in Fig. 9; the 1665 MHz histogram is very narrow while the 1667 is considerably broad (about twice that of 1665 MHz).

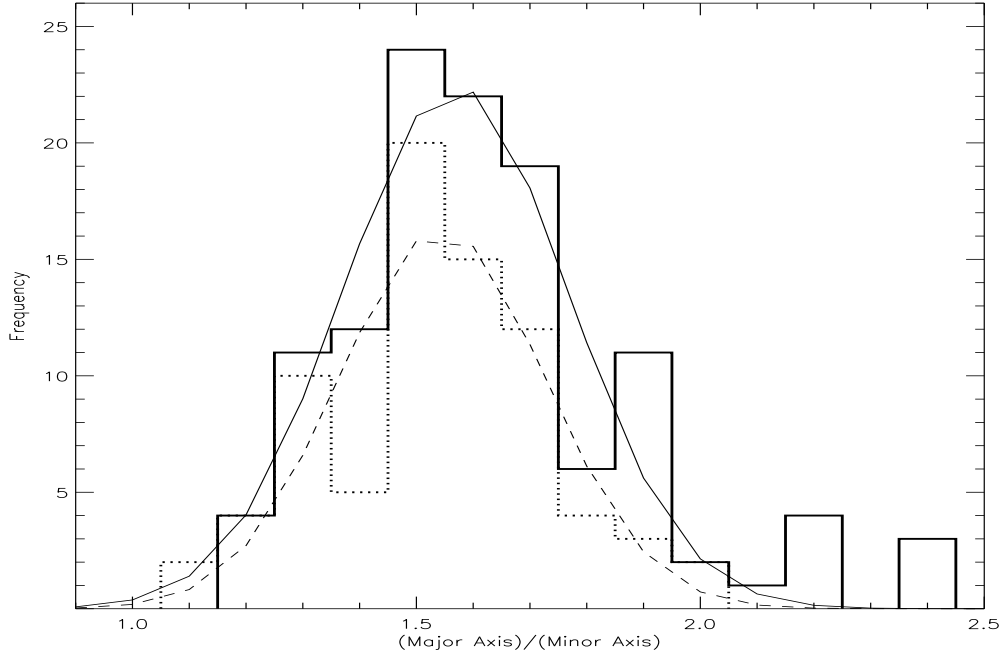


Fig. 11. Histograms of the Major Axis/Minor Axis ratio for the 1667 MHz spots (continuous line) and for the 1665 MHz spots (dotted line). The fitted Gaussians are as in Fig.8

8.2. Relation between the Maximum flux with PA and with Major and Minor axes

In Fig.13 the orientation of the principal axis, the major axis and the minor axis are plotted versus the Maximum flux (Peak) of each spot. It may be seen that the three variables converges to given values as the peak of the spots increases. The M/m ratio shows a similar behaviour. The data dispersion of the widths of the lines decreases as the peak increases but do not converges to a given value. Nevertheless, the widths for strong peaks fall in a range that considerably shorter than the range for weak peaks.

8.3. Relation of Major and minor axes with PA

In Fig.12 the values of m for all the spots are plotted versus their PA s. It may be seen that there is no a clear correlation. Instead of that, for a given minor axis value there are PA s in a wide range of values. Nevertheless, for large minor axis values the PA values tend to be larger than those for small minor axis values. A similar behaviour is seen between PA and Major Axis. Since it is expected that PA can take values up to 120° (the angle perpendicular to the galactic plane) the above behaviour could restrict the values that Major and minor axes can take.

The largest value expected for minor axis, from the PA versus minor axis plot is about $43 \text{ mas} + \sigma_{\min} \approx 30 \text{ mas}$. Then the largest expected values of the minor axis correspond to the largest values observed.

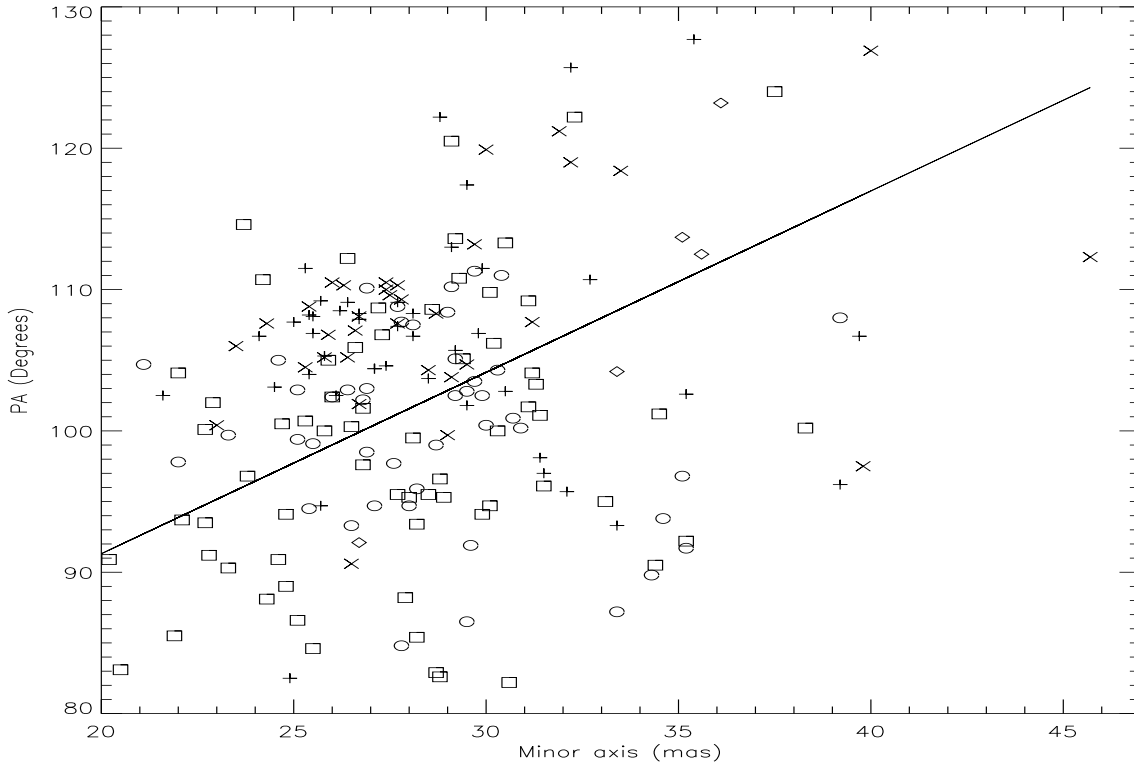


Fig. 12. The scatter plot of the PA and the minor axis of all the spots. *Rectangles* are for LCP 1667 MHz, *ellipses* for RCP 1667 MHz, *plus* for LCP 1665 MHz, *product* for RCP 1665 MHz, *triangles* for LCP 1612 MHz, *rombs* for RCP 1612 MHz spots.

8.4. The PA , Major and minor axes through the line

In Fig.14 the peak, the orientation of the principal axis, the Major axis and the minor axis values at the channels of the spectral line of one of the strongest spot are plotted. it may be seen that the values considerably differ from one channel to other. For other spots the maximum values of PA , M and m are attained at the wings of the line. This coincides with previous observations interpreted as due to saturation effects (Fish et al., 2006). However, for some spots large Major axis values are observed at channels near the center of the line. Also, cases are observed where the Major axis grows to one size of the line and decreases to the other.

In Fig.14b the data for LCP (open circles) and RCP (filled circles) M and PA values for the channels of the line are shown. It may be seen that the behaviour of data of both polarizations may be fitted with a single straight line indicating that PA decreases as M grows. In the case of PA and M and PA and m (Fig.12) for all the spots, PA tends to have larger values as m grows. On the other hand, for the above spot the relation differs. It means, the behaviour of the $PA - m$ and $PA - M$ relations found when taking into account the values for the maximum flux differs from that for different channels of a single spectral line. This probably is due to some other factor.

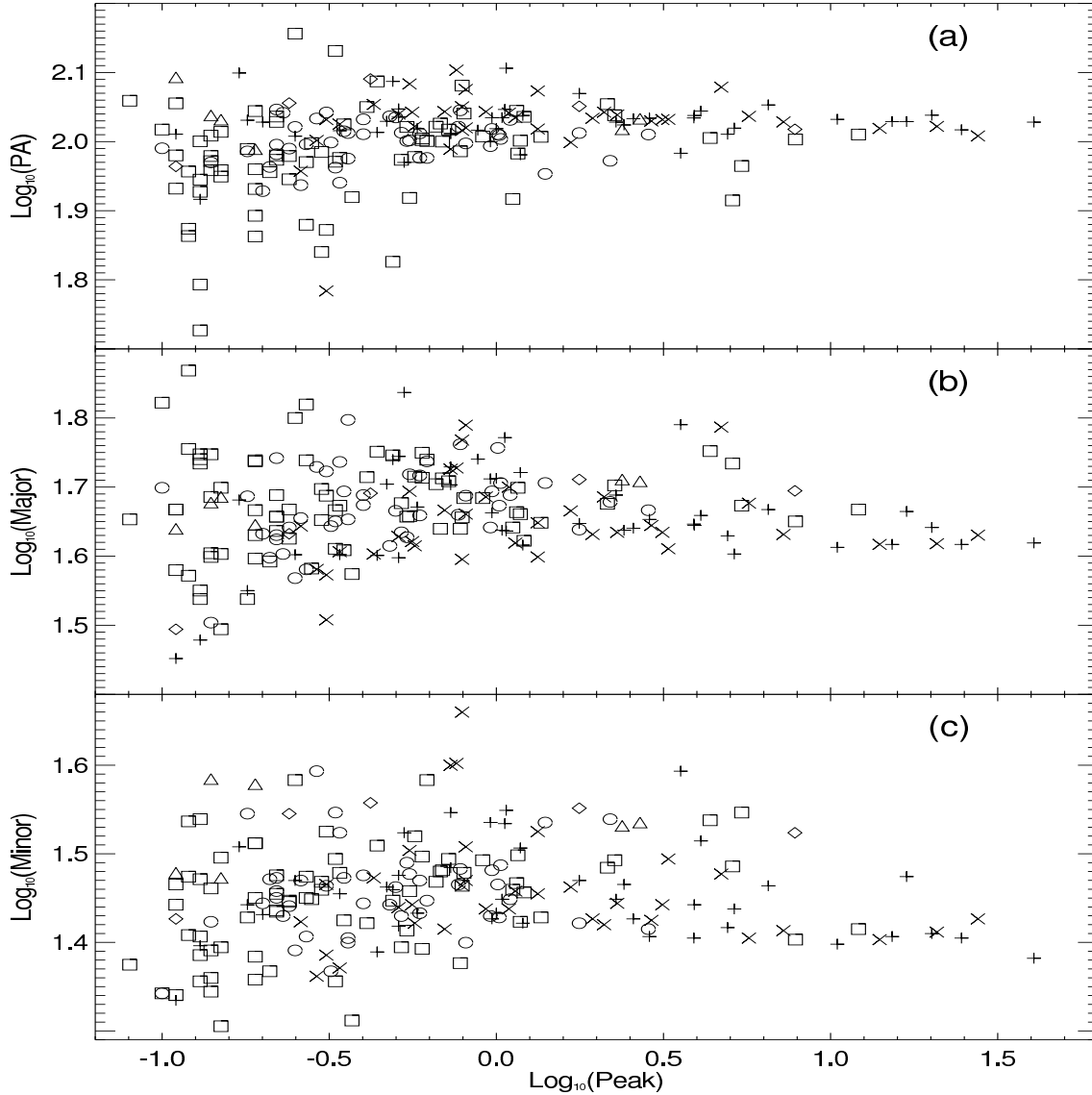


Fig. 13. Scatter plot of $\text{Log}(PA)$ against $\text{Log}(\text{peak})$, where peak is the maximum flux of each spot. It is clear that the data dispersion is larger for weak peaks and that high maxima converge towards a value of about 107 degrees. *Rectangles* are for LCP 1667 MHz, *ellipses* for RCP 1667 MHz, *plus* for LCP 1665 MHz, *product* for RCP 1665 MHz, *triangles* for LCP 1612 MHz, *rombes* for RCP 1612 MHz spots.

9. Density inhomogeneities and scattering parameters

It may be seen that, in spite of the fact that the maser spots are near to different HII regions and are forming different structures, all of them are oriented about the same angle (PA), nearly perpendicular to the galactic plane (Fig.15). This takes place even for distant spots. Some large scale parameter seems to orient the spots at preferential PA s, perpendicular to the galactic plane. This could be the result of an scenario as that proposed by Desai et al. (1994) where the density inhomogeneities are elongated along an ordered component of the galactic magnetic field (parallel to the galactic plane) and the

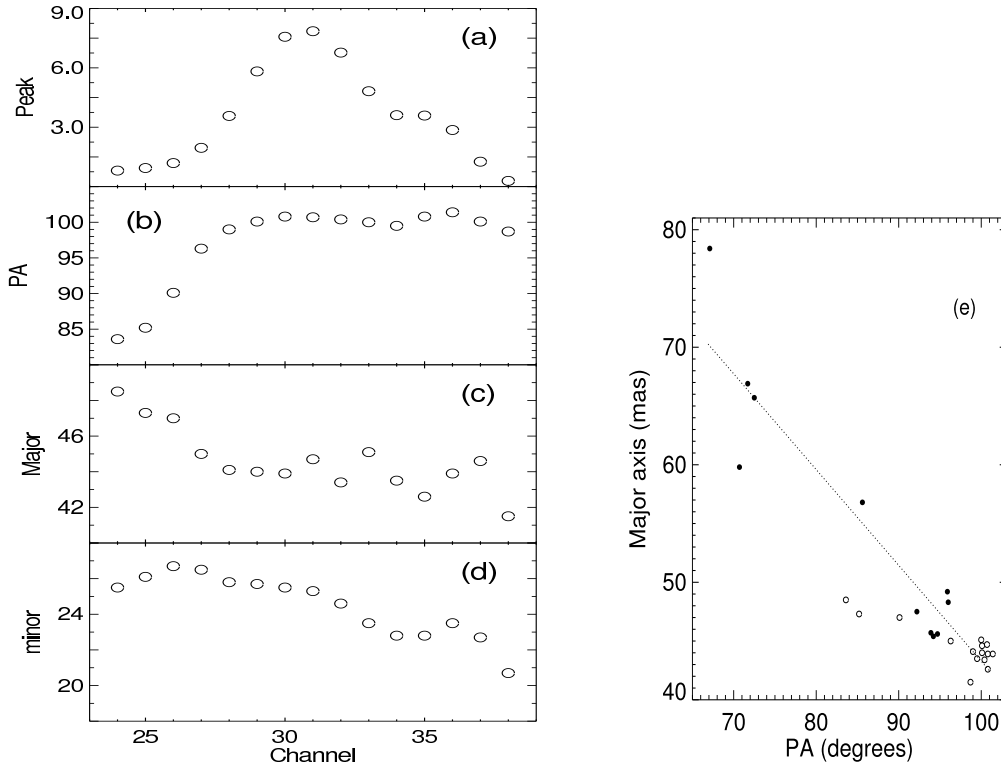


Fig. 14. **a)** The peak, PA , Major Axis and minor Axis, for the different channels of one of the strongest spot as was observed at LCP 1667 MHz. This spots also was detected at RCP 1667 MHz. **b)** The Major axis and PA for the spot as observed at the different channels where it was detected. Open circles are for LCP 1667 MHz and closed circles for RCP 1667 MHz data.

scattering by these inhomogeneities lead to an observer to record ellipses whose Major axis is perpendicular to that magnetic field (perpendicular to the galactic plane). Also, the present data clearly show a different behavior of PA , Major and minor axes with frequency and with polarization. The statistics of the differences in these parameters could be used to see if they could be explained in the frame of a structure function for a power law spectrum of density inhomogeneities of the interstellar plasma. The three-dimensional power spectrum of the electron density inhomogeneities may be a function of the type

$$P(q) = C_n^2 q^\beta \quad (2)$$

where C_n^2 is the strength of the turbulence, $q = \frac{2\pi}{\lambda}$ is the spatial wavenumber, and β is the law exponent.

For a Kolmogorov wavenumber spectrum of the density inhomogeneities the index is 11/3.

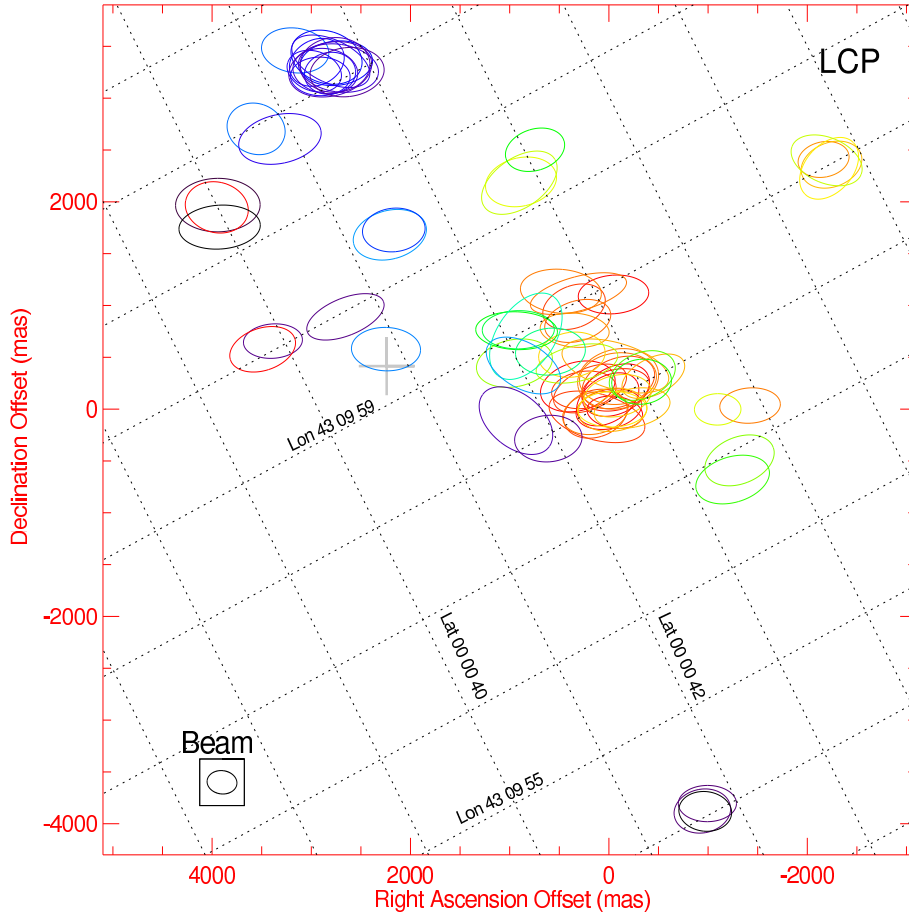


Fig. 15. Distribution of LCP 1667 MHz spots. The locations are denoted by ellipses whose sizes are multiplied by a factor of 15. As in Fig.1 the colors are proportional to the spots velocities. A grid of lines of constant Galactic Longitude and constant Galactic Latitude are shown as dotted lines. The CE of Gwinn et al. (1992) is denoted by +.

9.1. Coherence scale and Fresnel scale

In this section we use MKS units for the turbulence parameters, as was done in previous works. The mean apparent size of Major axis at 1667 MHz is 45.9 mas (Table2). The effective angle of dispersion (θ_o) is (Rickett, et al. 1984)

$$\theta_o = \frac{\theta_{app}}{\sqrt{4 \ln 2}} \quad (3)$$

The coherence scale

$$S_o = \frac{\lambda}{2\pi\theta_o} \quad (4)$$

results

$$S_o = 2.1 \cdot 10^5 m \quad (5)$$

which is less than the expected inner scale of the order of 10^9 m.

The Fresnel scale,

$$R_f = \sqrt{\frac{\lambda L}{2\pi}} \quad (6)$$

where L is the distance to the source. Using a distance of $L=11.4$ kpc, results

$$R_f = 3.2 \cdot 10^9 m \quad (7)$$

9.2. Scattering measure

The apparent angular size (θ_s) of a point source due to scattering is related to the strength of scattering (C_n^2), via the scattering measure (SM)

$$SM = \int_0^L C_n^2 ds \quad (8)$$

with SM given in $\text{kpc m}^{20/3}$.

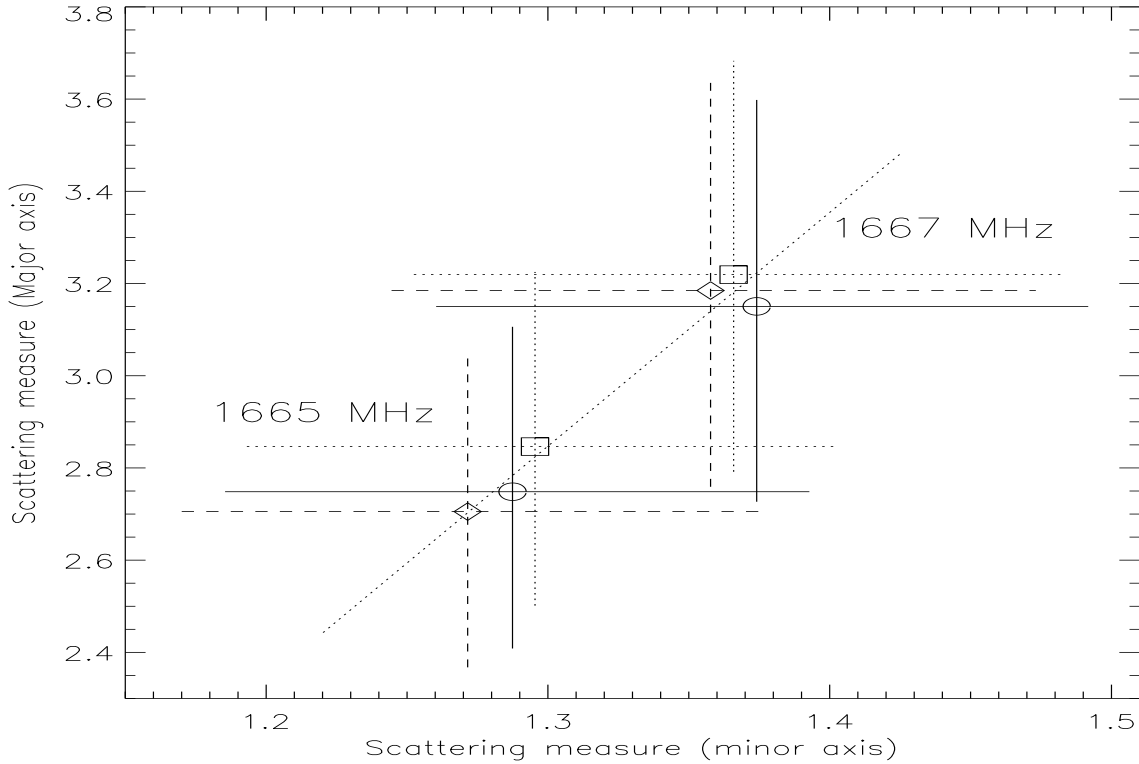


Fig. 16. The scattering measure computed based on Eq.8 and using the values of Table 2. The circles denote the scattering obtained for the mean values of $LCP + RCP$ data, the squares the scattering for LCP data and rombes for RCP data. The crosses extent to the extreme values obtained from the standard deviations (Eq. 11 for Major (vertical line) and minor axis (horizontal line)). Continuous line is for $LCP + RCP$ polarization, dotted line for LCP and dotted line for RCP . The dotted tilted line is the fitted straight line to the mean values.

If the scattering is constant along the scattering layer of thickness L then

$$SM = C_n^2 L \quad (9)$$

For a Kolmogorov spectrum and galactic sources Eq.8 is (Taylor and Cordes, 1993)

$$SM = \left(\frac{\theta_s}{71 \text{ mas}}\right)^{5/3} \nu_{GHz}^{11/3} \quad (10)$$

where θ_s is given in mas and ν is the frequency given in GHz. Using the mean values of Major and minor axes at 1665 MHz and 1667 MHz from Table 2 we may estimate the scattering measure to have an idea of the relation between the scattering at different frequencies, different polarizations and different axes. If we take into account the standard deviations then the extreme values are related to

$$\theta = \theta_{\text{mean}} \pm \sigma \quad (11)$$

which leads to the data plotted in Fig. 16. As may be seen from Fig.16, the difference between the scattering measure is large between 1665 MHz and 1667 MHz. Besides this difference there are two more differences, revealed by the different apparent sizes that have to be pointed out: 1. - A difference between the scattering at *LCP* and *RCP* polarizations at a given wavelength. 2. - A difference between the scattering for a given wavelength at angles roughly parallel to the magnetic global field (minor axis) and the scattering at angles perpendicular to it (Major axis).

We have fitted a line to the of *LCP*, *RCP* and *LCP + RCP* mean values of major and minor axes plotted in Fig.16. The slope of the fitted line results to be 5.1. This value reflects the difference in scattering between the Major and minor axis. Adopting a Kolmogorov wavenumber spectrum we could say that the scattering at the Major axis is about five times stronger than the scattering at the minor axis.

9.3. Structure function

The wave structure function is related to the power spectrum by (Moran et al. 1990)

$$D(r) = 8\pi^2 r_e^2 \lambda^2 L \int_0^\infty [1 - J_0(qr)] P(q) q dq \quad (12)$$

where r_e is the classical electron radius, $2.82 \cdot 10^{-15} \text{ m}$, λ is the observing wavelength, r is the distance between two points at the observer plane, L is the thick of the scattering screen.

In a power law spectrum there is an outer length scale at which energy is input and an inner scale at which dissipation of energy takes place. The inner scale has been estimated to be 10^{11} cm (Coles et al., 1987) but smaller values have also been estimated (Armstrong et al. 1981).

If the electron density fluctuations follow a power law function then the visibility function is related to the structure function and it is possible to estimate the index.

We have fitted Gaussian functions to the flux across each spot and the fits are quite good. In that case, the visibility also follows such a distribution. For an index $\beta \leq 4$ the

structure function may be estimated in the case of a Kolmogorov turbulence as follows (Moran et al. 1990)

$$D(r) = 8\pi^4 r_e^2 \lambda^2 L C_n^2 \frac{q_0^{4-\beta}}{4-\beta} r^2 \quad (13)$$

where q_0 is the inner scale and r is the distance between two points at the observer plane.

The line of sight from W49N has a long path and it is expected that rays from the source intersec many scattering clumps. Estimations of the distance and the thick of the scattering layer suggest that the scattering material may be considered nearly uniformly distributed along lines of sight a few Kiloparsecs long but the thickness could be considerably shorter (Gwinn et al. 1993).

Lets assume that $D(r) = \frac{1}{2}$ for a spot size θ that takes place for a baseline r given by

$$\theta = \frac{\lambda}{r} \quad (14)$$

We may express the strength of turbulence and the inner scale as a set of constants and the wavelength, the distance at the observing plane (r) and the screen thick (L) as

$$C_n^2 \frac{q_0^{4-\beta}}{4-\beta} = \left(16\pi^4 r_e^2 \lambda^2 L r^2 \right)^{-1} \quad (15)$$

Further we make an attempt to estimate the structure function based on the mean values at the histograms.

then we can write the left hand side of Eq.15 in terms of the size of the spot and the wavelength

$$\frac{\theta^2}{A \lambda^4} = C_n^2 \frac{q_0^{4-\beta}}{4-\beta} L \quad (16)$$

where A is a constant ($1.24 \cdot 10^{-26} \text{ m}^2$) and L is the scattering screen thickness.

If the right hand side of Eq.16 would be constant then one would have the typical case where the apparent size varies as the wavelength to the square due to scattering.

Table 2. Mean Major and minor axes and $\frac{\theta^2}{A \lambda^4}$ (in 10^{15} , $\text{rad}^2 \text{ m}^{-6}$)

ν	L	R	LR	F(L)	F(R)	F(LR)	LR(peak)
	Major axis (mas)						
1665	43.3	42.0	42.4	3.37	3.17	3.23	40.7
1667	46.5	46.2	45.9	3.91	3.86	3.81	
	Minor axis (mas)						
1665	27.0	26.7	26.9	1.31	1.28	1.30	25.1
1667	27.8	27.7	27.9	1.40	1.39	1.41	

In Table 2 the Major and minor mean values are given in mas. The estimates of the left hand side of Eq.16 using these values as θ are given in columns 5th to 7th. The last

column correspond to the values to which Major and minor axes converges as the peak of the spot grows (Fig.13). The columns 5th to 7th are related to the scattering parameters, since they are obtained substituting $\frac{\theta^2}{A\lambda^4}$ which, according to Eq.16 corresponds to

$$C_n^2 \frac{q_0^{4-\beta}}{4-\beta} L \quad (17)$$

Lets assume that $\beta = \frac{11}{3}$, the index for Kolmogorov turbulence. Then, using the value for $L + R$ of Table 2, obtained based on the Major axis at 1667 MHz, we may estimate the strength of turbulence, C_n^2 , from

$$3C_n^2 q_0^{1/3} L = 3.81 \cdot 10^{15} \quad \text{or} \quad C_n^2 q_0^{1/3} L = 1.27 \cdot 10^{15} \quad (18)$$

which leads to

$$C_n^2 = \frac{1.27 \cdot 10^{15}}{q_0^{1/3} L} \quad (19)$$

If $q = 10^9$ m then

$$C_n^2 = \frac{1.27 \cdot 10^{15}}{10^3 L} \quad \text{or} \quad C_n^2 = \frac{1.27 \cdot 10^{12}}{L} \quad (20)$$

The values for C_n^2 are of the order of 10^{-4} to 1 (Cordes et al., 1984) or 10^4 to 10^6 Moran et al, (1990). From Eq. 20 it may be seen that we would need that the scattering thick layer would be of the order of 10^6 m to 10^{16} m to obtain these values, which is considerably shorter than the distance to the source ($4.3 \cdot 10^{20}$ m).

9.4. Apparent spot size at different wavelengths

If the apparent size would vary as the wavelength to the square then we would expect that it would be larger for spots at 1665 MHz ($M(1665)$) than at 1667 MHz ($M(1667)$). In that case, $\frac{M(1665)}{M(1667)} = 1.002$ Substituting the values found for $M(1665)$ and $M(1667)$ (Table 2) we have that $\frac{M(1665)}{M(1667)} = 0.6$ The expected ratio is larger than the unity and instead of that the observed one is smaller than unity. Since the 1667 MHz data is considerably more spread than the 1665 MHz one then, the expected ratio could accomplish only for some particular cases.

9.5. Standard deviation of M , m and λ

No correlation was found neither between M and the central wavelength (λ) nor between m and the central λ for the spots at 1667 MHz and at 1665 MHz. On the other hand, as may be seen from 3 the standard deviation of the Major and minor axes between the spots of a given frequency, relative the mean values at the same frequency, are of the order of 10^{-1} . On the other hand, the standard deviations of λ of different spots at the given frequency, also relative to the mean values, are of the order of 10^{-5} - 10^{-4} . Taking

into account that there is no correlation between the apparent size and λ we expect that large (or small) apparent sizes do not necessarily correspond to large (or small) λ of the above mentioned ranges (any value of M may take place for any λ). Then, the $\frac{\theta^2}{\lambda^4}$ ratio is not constant even for the spots of a given frequency. It means, either the parameters of the right hand side of Eq.16 vary from one spot to other or this equation does not express the observed density inhomogeneities. Probably, the scattering that led to the observed apparent sizes does not correspond to that of Eq.16.

9.6. Variations of apparent size and variations of the strength of turbulence

The differences observed in the apparent size of spots at different frequencies, different polarizations and at different axis (Major and minor axes) could be due to different scatterings. To estimate the differences in scattering that would lead to these differences we further use the relative σ respect the mean values of Major and minor axes. In this case we do not need to estimate the absolute values of scattering.

Using Eq.16 we may write

$$F = A L \lambda^4 \left[C_n^2 \frac{q_o^{4-\alpha}}{4-\alpha} \right] \quad (21)$$

where $F = \theta^2$ is the function that contains the variables that, after the above assumptions and simplifications, describe the turbulence.

The right hand side of Eq.21 is not necessarily constant. Moreover, we may attribute the differences in the apparent size to variations of F .

Table 3. Relative standard deviation (σ/θ_{mean}) for Major and Minor axes data

ν	L	R	LR	$\frac{\sigma_F}{F}$		
Major axis						
1665	0.09	0.07	0.10	0.008	0.005	0.010
1667	0.14	0.12	0.14	0.020	0.014	0.020
Minor axis						
1665	0.09	0.08	0.09	0.008	0.006	0.008
1667	0.14	0.08	0.12	0.020	0.006	0.014

In the columns 2-4 of Table 3 the relative mean values of Major and Minor axes σ/θ_{mean} are given. In the last three columns the ratio $\frac{\sigma_F}{F}$ that corresponds to these columns (since $F = \theta^2$).

The values for $\frac{\sigma_F}{F}$ are very similar for the relative standard deviation of the apparent size respect the mean values. The variations for Major axis data are of $\approx 10^{-2}$ for 1665

MHz and $\approx 2 \cdot 10^{-2}$ for 1667 MHz. For minor axis data the values are similar ($8 \cdot 10^{-3}$ for 1665 MHz and $1.4 \cdot 10^{-2}$ for 1667 MHz).

It means, the variations of the apparent size are explained by small relative variations of F (of 1-2 %) and possible small variations of the strength of turbulence.

9.7. Strengths of turbulence for the directions of Major and minor axes

If we want to estimate the difference of F for Major axis respect the minor axis we have to use the data for the M/m ratio of each spot. In Table 9.7 the mean values of these ratios are given. In the last three columns the $\frac{F_M}{F_m}$ ratios are given (also computed simply with $F = \theta^2$).

Table 4. Mean values of the spot by spot Major/minor ratio

ν	L	R	LR	$\frac{F_M}{F_m}$		
	Major/minor					
1665	1.56	1.52	1.55	2.43	2.31	2.40
1667	1.57	1.56	1.57	2.46	2.43	2.46

It is clear that the ratios of F for Major and minor axes are of about 2.4. Since the value of F for the Major axis is about 2.4 that for the minor axis then the strength of turbulence could considerably differ from one direction to the other. This indicates that the scattering is not isotropic.

9.8. The M/m mean ratios and scattering at different axes

As has been shown before (Fig.11) the mean values for the histograms of M/m for 1665 MHz and 1667 MHz ratios are very similar to each other. This indicates that the difference in scattering from one axis to other does not depend on the frequency.

The ratio $\frac{\theta_M}{\theta_m}$ says how anisotropic the scattering is. According to the ratios found at 1665 MHz and 1667 MHz, the anisotropy is almost constant with frequency. Nevertheless, the scattering considerably differs from one axis to another.

The $\frac{\theta_{M_{mean}}}{\theta_{m_{mean}}}$ ratio computed using mean values is slightly larger, in all the cases, than the ratios computed spot by spot (Table 9.7). This indicates that the statistics reproduces well the situation for a given spot. However, the fact that in all the cases the ratio using mean values is larger indicates that there is some bias in the distribution and the ratio of the mean Major axis relative the mean minor axis is slightly larger than the ratio of the axis for each spot. In other words, the mean value of the Major axis, for some statistical reason, is larger than the value obtained spot by spot.

9.9. The $\frac{M(1667)}{M(1665)}$ and $\frac{m(1667)}{m(1665)}$ ratios

To better understand the behaviour of the scattering it is important to know how the scattering behaves with frequency. With this aim we use the mean values of the histograms to estimate the ratio of the Major axis at 1667 MHz respect that at 1665 MHz and the same for the minor axis.

Table 5. Ratios of the mean values of Major (M) and minor (m) axes

Axis	$\frac{1667(L)}{1665(L)}$	$\frac{1667(R)}{1665(R)}$	$\frac{1667(LR)}{1665(LR)}$	$\frac{F_{1667}}{F_{1665}}$		
M	1.07	1.10	1.08	1.14	1.21	1.16
m	1.03	1.04	1.04	1.06	1.08	1.08

In Table 9.9 the ratios of the M and m mean values and the estimated $\frac{F_{1667}}{F_{1665}}$ ratios are given.

It is clear that, for the major axis the $\frac{F_{1667}}{F_{1665}}$ ratios are larger than for the minor axis. This means that from 1665 MHz to 1667 MHz the Major axis increases more than the minor axis. This produces that, for the mean values, the ellipses at 1667 MHz would be more ellongated than those at 1665 MHz. This result also indicates that the scattering is not isotropic.

9.10. Anisotropic turbulence

From the above results, it seems that the scattering considerably differs from one axis to another. Theoretical works indicate (Higdon, 1986) that the presence of a magnetic field will make the turbulence spectrum two-dimensional, in such a case the scattering inhomogeneities would be elongated parallel to the magnetic field and scattering would also be anisotropic.

We may consider that the ratio $\frac{\theta_M}{\theta_m}$ says how anisotropic the scattering is. On the other hand, the fact that $M/m = \text{constant}$ indicates that the difference in scattering from one axis to other does not depend on the frequency. It means, for our field of view the anisotropy can be considered constant.

Narayan and Hubbard (1988) express the anisotropic power law spectrum for density inhomogeneities due to turbulence as

$$Q = Q_0(\rho^2 q_x^2 + q_y^2)^{-\frac{\rho}{2}} \quad (22)$$

where ρ is the degree of anisotropy and q_x , q_y are the wavenumbers in x and y directions, respectively.

The observed, or apparecnt size of the maser spots, depend on the elements l_x and l_y of the Jacobian that describes focusing and defocusing due to inhomogeneities. If l_x (or l_y) > 1 the rays are focused and for l_x (or l_y) < 1 the rays are defocused.

Narayan and Hubbard (1988) show that, under the appropriate assumptions, the major axis of the apparent source becomes at the direction where an inhomogeneity is shorter while, the minor axis is observed at the direction where it is larger. The apparent x and y sizes of point sources are

$$\theta_x = l_x^2 \theta_{x0} \quad \text{and} \quad \theta_y = l_y^2 \theta_{y0} \quad (23)$$

where θ_{x0}/L and θ_{y0}/L are the half angles along x and y axis, respectively, of the cone of rays scattered by the inhomogeneities.

The M/m ratio may be related to the indexes of focusing and/or defocusing as follows

$$\frac{\theta_y}{\theta_x} = \frac{l_y^2}{l_x^2} \frac{\theta_{y0}}{\theta_{x0}} \quad (24)$$

where the $\frac{\theta_y}{\theta_x}$ would be M/m . Assuming that θ_x and θ_y do not vary then the variations observed would be due to variations of the $\frac{l_y^2}{l_x^2}$ ratio. The dispersion of the ratio at low values of the peak may be interpreted, in the frame of the Narayan and Hubbard (1988) description of anisotropic scattering, as a result of variations of the l_y^2 and l_x^2 parameters.

The fact that the M/m ratio has a larger dispersion for small values of the peak flux of the spot (Fig.13) indicates that to smaller M values does not necessarily correspond smaller m values. It means, for weak spots the M value does not lead to restrictions for the m value. This implies that there is a weak or no dependence between M and m for weak spots. However, the dispersion of the M/m ratio decreases as the peak flux of the spots grows. In other words, as the flux grows the M and m values, respectively, approach to given values. This also makes to M and m to seem dependent to each other; at strong spots, given the M value the m one is more determined than for weak spots.

Silantiev et al. (2006) found that the optical depth (τ) increases with turbulence. Since for maser emission τ is negative then the turbulence increases the effect of amplification. It means, the maser emission becomes stronger when the outgoing radiation crosses a turbulent medium. Then, scattering of the emission for large peak values could be considered near saturation???. We can say that Fig.13 reveals different levels of scattering. For weak scattering (at low peak values) the data dispersion is large because the scattering at one axis is weakly related to the scattering at the other axis. For strong spots the scattering at one axis is more related to the scattering at the other axis leading to the M/m ratio to converge.

10. Discussion

Velocity gradients have been observed in other OH sources (Fish et al. 2006). However, the velocity gradients at the small arc and at the jet are seen together with magnetic field gradients. A velocity gradient does not necessarily implies a magnetic field gradient since the magnetic field depends on the velocity difference between the two polarization,

but not on the value of one of the velocities. The large arc also shows a velocity gradient but the magnetic field seems to be inhomogeneous and probably could be the result of turbulence. In this case, the velocity gradients could be explained if the spots are in a velocity field such as a turbulent eddy. However, the size of such an eddy would have to be of the order of 4000 AU. It has been found that the PA takes similar values even for quite separated spots. On the other hand, the PA, major axis and minor axis show clear differences from one frequency to other. Also, a remarkable difference is seen between the Major and minor axes values. The above results indicate that the magnetic field seems to be playing an important role at both the small scale structures and the behaviour of the spots over a large scale. A magnetic field would lead to an anisotropic velocity field (Higdon 1986) that would lead to density anisotropies. The difference between the Major and minor axes, in principle could be explained with two different inner length scales of the power spectrum, along and perpendicular to the magnetic field. Anisotropic scattering could lead to both, differences from one wavelength to another and differences from one polarization to the other. However, the differences of the apparent sizes from one frequency to other are larger than the expected due to scattering. Also, large differences are seen for PA. Probably there is some effect due to Faraday rotation on the behaviour of the spots parameters with frequency. According to Shebalin et al. (1983) the anisotropy is greater at the higher wave numbers. Then, it is expected that the anisotropy will be larger for 1667 MHz than for 1665 MHz, as observed for the apparent sizes in our case.

11. Conclusions

At the three frequencies more spots at LCP than at RCP were detected. Some structures are outlined by the spots. The magnetic field at some of them could be estimated. For two structures (the small arc and the jet) a velocity and a magnetic field gradient are observed. Based on the histograms of the spots parameters, differences in the data were found for different frequencies as well as for different polarizations. Estimations of the turbulence parameters give different values for: 1) The different frequencies, 2) the different polarizations and 3) for the different axes. The largest difference was found between Major and minor axes.

A three dimensional power spectrum of density inhomogeneities was used and the differences of the parameters between the frequencies and between the axes could be not explained which indicates that the turbulence is not isotropic.

Acknowledgements.

References

- Armstrong, J. W., Cordes, J. M., and Rickett, B.J. 1981, *Nature*, 291, 561
 Coles, W.A., Frehlich, R.G., Rickett, B., and Codona, J.L. 1987, *ApJ*, 315, 666

- Cordes84 Cordes, J. M., Ananthakrishnan, S., and Dennison, B. 1984, *Nature*, 309, 689
- Fish, V.L., Briske, W.F, Sjouwerman, L.O. 2006, *ApJ*, 647, 418
- Gwinn, C.R., Bartel, N., and Cordes, J.M. 1993, *ApJ*, 410, 673
- Gwinn, C.R., Moran, J.M., Reid, M. 1992, *ApJ*, 393, 149
- Kent, S. R. Mutel R. L. 1982, *ApJ* 263, 145
- Diamond, P. J., Martison, A., Booth, R. S., Winnberg, A. 1988, *Radio Wave Scattering in the Interstellar Medium*, AIP Conference Proceedings 174, New York, AIP, p. 195
- Higdon, J.C. 1986, *ApJ*, 309, 342
- Moran, J. M., Rodriguez, L. F., Greene, B., Backer, D.C. 1990, *ApJ*, 348, 174
- Narayan, R., Hubbard, W.B. 1988, *ApJ*, 325, 503
- Rickett, B.J., Coles, W. A., Bourgois, G. 1984, *A&A*, 134, 390
- Rickett, B.J. 1990, *ARA&A*, 28, 561
- Shebalin, J. V., Matthaeus, W. H., Montgomery, D. 1983, *J. Plasma Phys.*, 29, 525
- Silant'ev, N.A., Lekht, E.E., Mendoza-Torres, J.E., Rudnitskij, G.M. 2006, *A&A*, 453, 989
- Taylor, J.H. Cordes, J.M. 1993, *ApJ*, 411, 674

12. Appendix A

Table 6. W49N 1612 MHz LCP Maser Parameters

Feature	Vel (km s ⁻¹)	Width (km s ⁻¹)	Peak (Jy Beam ⁻¹)	$\Delta\alpha$ (mas)	$\Delta\delta$ (mas)	PA (Degrees)
1.....	20.6	0.6	0.2	-596.2	-590.0	170.1
2.....	16.5	1.1	0.1	-184.5	102.9	6.4
3.....	16.0	0.8	0.1	-28.4	-893.5	171.6
4.....	15.0	0.5	2.7	-9.5	15.1	170.4
5.....	14.1	0.5	2.4	-0.7	0.8	166.7
6.....	13.4	0.6	0.2	18.6	-35.9	160.0

Table 7. W49N 1612 MHz RCP Maser Parameters

Feature	Vel (km s ⁻¹)	Width (km s ⁻¹)	Peak (Jy Beam ⁻¹)	$\Delta\alpha$ (mas)	$\Delta\delta$ (mas)	PA (Degrees)
1.....	18.9	0.6	0.2	-582.5	-594.4	113.7
2.....	17.1	0.8	0.1	-184.6	106.5	92.1
3.....	15.7	0.7	1.8	-9.4	15.2	112.5
4.....	14.8	0.5	7.8	0.0	0.1	104.2
5.....	14.1	0.5	0.4	19.5	-34.7	123.2

Table 8. W49N 1665 MHz LCP Maser Parameters

Feature	Vel (km s ⁻¹)	Width (km s ⁻¹)	Peak (Jy Beam ⁻¹)	$\Delta\alpha$ (mas)	$\Delta\delta$ (mas)	PA (Degrees)
1.....	21.1	0.4	4.9	45.7	25.3	165.0
2.....	21.0	0.4	40.6	-0.5	-0.3	169.2
3.....	20.3	0.3	0.4	-929.9	-1107.7	165.6
4.....	19.8	0.4	1.0	105.0	-318.7	170.8
5.....	19.7	0.5	0.5	-52.3	798.1	174.0
6.....	19.6	0.5	4.2	379.8	1297.1	139.0
7.....	19.6	0.4	0.5	164.7	823.0	172.5
8.....	19.4	0.5	0.1	161.2	-751.3	165.0
9.....	19.3	0.6	0.3	537.1	1138.0	166.2
10.....	19.3	0.4	1.0	-360.4	-13.0	170.8
11.....	18.7	0.5	2.4	179.8	-35.9	168.2
12.....	18.8	0.8	0.9	-21.7	734.8	53.0
13.....	18.3	0.4	20.1	-26.8	720.7	171.7
14.....	18.1	0.5	10.5	175.5	-28.7	170.2
15.....	17.7	0.3	1.0	557.3	1182.6	166.9
16.....	17.7	0.6	0.6	174.2	-91.5	166.9
17.....	17.7	0.5	0.5	-378.0	-68.4	171.0
18.....	17.6	0.6	2.9	-51.6	745.2	170.6
19.....	16.9	0.6	24.6	176.7	-44.9	166.5
20.....	15.8	0.6	15.3	172.8	-26.9	169.4
21.....	15.7	0.5	6.5	-5.4	839.9	175.5
22.....	15.1	0.8	0.7	985.7	443.9	165.3
23.....	14.6	0.4	2.6	585.4	433.8	170.4
24.....	14.2	0.4	0.2	-1285.2	-479.2	169.9
25.....	13.8	0.4	4.1	987.1	2069.3	173.2
26.....	13.6	0.6	0.4	902.9	65.5	9.6
27.....	13.2	0.5	0.2	-329.1	903.2	164.3
28.....	12.1	0.5	16.9	954.0	2196.7	169.4
29.....	11.9	0.4	1.2	292.7	498.2	171.6
30.....	11.8	0.7	1.8	624.2	572.0	179.9
31.....	11.7	0.3	3.9	287.8	546.5	170.7
32.....	11.1	0.5	5.2	655.2	462.2	167.1
33.....	9.4	0.5	3.9	676.1	481.0	171.6
34.....	8.2	0.6	2.3	880.2	410.4	169.2
35.....	7.8	0.5	1.1	657.0	454.7	37.9
36.....	5.7	0.7	1.1	3356.3	2617.2	173.8
37.....	5.2	0.5	3.5	2808.4	3286.1	153.6
38.....	5.0	0.9	1.0	3365.3	2650.7	162.4
39.....	4.8	0.4	1.2	2675.5	3259.4	158.2
40.....	4.1	0.6	0.2	675.7	246.0	8.2

.

Table 9. W49N 1665 MHz RCP Maser Parameters

Feature	Vel (km s ⁻¹)	Width (km s ⁻¹)	Peak (Jy Beam ⁻¹)	$\Delta\alpha$ (mas)	$\Delta\delta$ (mas)	PA (Degrees)
1.....	21.2	0.4	0.7	14.4	118.8	173.0
2.....	20.0	0.5	2.1	-36.1	727.9	172.8
3.....	19.5	0.3	5.7	-138.4	932.8	171.3
4.....	18.5	0.6	0.6	-548.3	909.0	172.8
5.....	18.2	0.4	0.8	-12.2	848.9	1.5
6.....	18.2	0.5	14.0	175.5	-28.6	167.0
7.....	17.5	0.5	2.9	-51.2	745.2	169.6
8.....	17.0	0.5	27.6	179.0	-42.0	164.4
9.....	16.3	0.5	0.8	-24.0	929.9	174.8
10.....	16.3	0.5	1.3	-28.5	894.6	0.9
11.....	15.8	0.5	20.8	173.2	-27.0	167.7
12.....	15.3	0.4	2.3	-51.3	889.9	171.8
13.....	15.1	0.4	7.2	-966.6	179.6	169.3
14.....	14.8	0.4	0.3	-209.2	757.1	168.5
15.....	14.7	0.4	0.9	-344.0	776.2	173.0
16.....	14.0	0.4	0.6	-337.9	822.2	167.7
17.....	13.3	0.4	1.1	-1384.2	50.0	170.7
18.....	13.1	0.5	0.3	-698.0	-532.8	170.1
19.....	13.0	0.4	1.9	-1161.7	-750.6	170.6
20.....	12.6	0.4	0.8	990.4	453.6	167.2
21.....	12.3	0.4	0.8	950.8	2187.7	9.4
22.....	12.1	0.5	0.3	624.6	560.2	153.1
23.....	11.9	0.4	1.1	869.8	2462.4	172.5
24.....	11.2	0.5	1.3	655.2	460.8	166.8
25.....	10.9	0.5	3.1	585.7	435.6	170.1
26.....	10.4	0.4	4.7	872.6	704.9	2.4
27.....	9.9	0.4	0.6	989.6	2049.1	3.7
28.....	9.4	0.5	0.8	633.6	475.2	169.3
29.....	8.3	0.6	0.4	623.5	560.2	175.7
30.....	7.8	0.5	3.3	657.0	454.7	0.4
31.....	7.7	0.4	1.7	895.7	414.7	162.2
32.....	6.4	0.8	0.3	3458.9	-3467.9	123.3
33.....	5.7	0.4	0.5	678.2	482.0	172.1
34.....	3.6	0.4	0.7	2812.3	3278.5	160.0
35.....	1.1	0.4	0.3	2844.0	-1603.4	162.9

Table 10. W49N 1667 MHz LCP Maser Parameters

Feature	Vel (km s ⁻¹)	Width (km s ⁻¹)	Peak (Jy Beam ⁻¹)	$\Delta\alpha$ (mas)	$\Delta\delta$ (mas)	PA (Degrees)
1.....	20.8	0.4	0.7	313.2	219.3	166.6
2.....	20.6	0.5	0.8	11.4	94.7	3.0
3.....	20.3	0.5	0.5	-46.4	1106.3	156.6
4.....	19.7	0.7	2.2	-70.2	183.6	175.8
5.....	19.6	0.3	0.4	-59.7	-30.4	145.6
6.....	19.3	0.6	7.8	-0.2	0.4	163.2
7.....	19.0	0.4	12.1	-67.8	185.8	164.9
8.....	18.8	0.3	0.8	252.1	185.9	159.3
9.....	18.7	0.6	0.4	190.1	199.2	174.7
10.....	18.6	0.4	0.2	351.3	988.2	171.2
11.....	18.6	0.5	0.3	120.1	-74.4	138.3
12.....	18.5	0.4	0.7	136.6	-44.2	168.7
13.....	18.4	0.5	2.3	-95.7	257.5	171.7
14.....	18.0	0.7	0.5	314.0	851.0	167.5
15.....	18.0	0.6	0.1	306.9	1114.6	166.6
16.....	17.8	0.4	0.2	483.8	1136.9	147.9
17.....	17.9	0.6	0.6	-93.0	291.8	162.7
18.....	17.8	0.6	1.4	137.3	-37.2	164.1
19.....	17.8	0.9	0.6	-91.4	294.5	157.5
20.....	17.9	0.6	0.3	-1423.1	34.6	156.0
21.....	17.6	0.7	0.1	-2164.3	2408.8	162.6
22.....	17.5	0.3	0.1	345.0	762.1	148.0
23.....	17.2	0.8	0.1	-65.5	416.5	137.3
24.....	17.0	0.4	0.1	-448.2	317.4	177.1
25.....	17.0	0.4	0.1	-36.8	-6.4	158.0
26.....	16.9	0.4	1.2	-2244.2	2358.7	171.1
27.....	16.9	0.4	0.6	-233.9	10.2	163.0
28.....	16.8	0.5	1.2	-87.0	129.1	162.8
29.....	16.6	0.7	0.3	373.0	525.2	159.1
30.....	16.4	0.7	0.2	-33.8	-1.6	153.7
31.....	16.3	0.4	0.3	-2220.1	2323.4	17.8
32.....	15.8	0.5	0.9	886.0	2192.4	164.2
33.....	15.6	0.4	0.2	-1096.9	-2.3	153.4
34.....	15.6	0.8	0.4	902.5	2184.5	4.7
35.....	15.4	0.6	0.3	-2194.9	2400.1	131.7
36.....	15.2	0.8	0.1	322.0	440.3	164.5
37.....	14.8	0.5	0.7	952.2	443.5	162.5
38.....	14.5	0.6	0.8	-1316.9	-494.3	172.3
39.....	14.0	0.4	1.1	-336.6	324.4	173.3
40.....	13.4	0.6	0.7	1247.4	670.2	167.6

Table 11. W49N 1667 MHz RCP Maser Parameters

Feature	Vel (km s ⁻¹)	Width (km s ⁻¹)	Peak (Jy Beam ⁻¹)	$\Delta\alpha$ (mas)	$\Delta\delta$ (mas)	PA (Degrees)
1.....	20.9	0.3	0.4	-6.6	55.5	165.4
2.....	20.8	0.5	0.3	-38.0	123.0	161.6
3.....	20.7	0.5	0.2	7.0	85.5	173.8
4.....	19.8	0.6	0.4	6.2	106.2	170.2
5.....	19.6	0.4	0.8	314.6	219.1	167.6
6.....	18.8	0.7	0.1	-68.1	178.5	155.9
7.....	18.5	0.4	0.5	-2243.2	2357.3	171.3
8.....	18.4	0.6	0.3	-61.6	-31.4	166.0
9.....	18.2	0.7	0.6	4.0	3.2	157.2
10.....	17.7	0.4	0.6	363.2	993.6	162.9
11.....	17.7	0.5	1.0	-174.5	301.6	166.8
12.....	17.6	0.3	0.2	251.3	188.2	158.4
13.....	17.6	0.5	0.2	194.1	197.1	167.5
14.....	17.3	0.6	0.8	127.4	-37.5	173.5
15.....	17.1	0.4	1.0	355.4	987.8	164.7
16.....	16.5	0.6	0.5	137.0	-36.7	165.5
17.....	16.5	0.4	0.8	314.1	851.4	161.9
18.....	16.2	0.4	0.2	369.7	807.1	154.4
19.....	16.1	0.4	0.4	-67.3	406.1	165.0
20.....	15.5	0.4	2.8	-86.6	128.9	164.9
21.....	15.3	0.5	0.2	368.3	528.1	161.5
22.....	15.2	0.5	0.3	-232.7	9.8	162.2
23.....	14.3	0.4	1.8	-1423.8	36.0	165.4
24.....	13.7	0.4	0.5	886.7	2191.3	162.7
25.....	13.6	0.5	0.5	-1258.6	-673.6	170.9
26.....	13.2	0.4	1.0	954.0	443.9	163.4
27.....	12.4	0.4	1.1	-336.9	325.9	170.0
28.....	11.6	0.6	1.0	920.2	767.5	165.0
29.....	10.4	0.4	0.3	844.2	689.0	172.7
30.....	9.5	0.6	0.2	578.2	549.0	172.6
31.....	8.7	0.4	0.6	896.0	2462.8	165.3
32.....	8.3	0.4	0.6	865.4	419.8	157.2
33.....	7.9	0.5	0.3	3186.7	3494.9	149.7
34.....	7.6	0.5	0.2	2207.9	1679.8	160.2
35.....	6.4	0.4	0.1	2195.6	539.6	160.4
36.....	6.4	0.5	0.2	2242.8	580.7	147.3
37.....	5.6	0.8	0.4	3296.2	532.4	157.0
38.....	4.9	0.5	0.3	3884.4	2557.8	170.5
39.....	4.7	0.6	0.2	3319.9	2602.4	159.3
40.....	4.7	0.5	0.2	2008.4	2311.6	149.0

Table 12. W49N 1612 MHz LCP Zeeman pairs

Vel (kms ⁻¹)	α off (mas)	σ (mas)	δ off (mas)	σ (mas)	Vel (kms ⁻¹)	α off (mas)	σ (mas)	δ off (mas)	σ (mas)	$\Delta\alpha$ (mas)	$\sigma(\alpha)$ (mas)	$\Delta\delta$ (mas)	$\sigma(\delta)$ (mas)	B mG
RCP 1612					LCP					RCP		LCP		
17.13	-184.6	1.6	106.5	1.4	16.46	-184.5	1.8	102.9	1.6	0.1	2.4	3.6	2.1	5.54
15.70	-9.4	0.2	15.2	0.1	15.00	-9.5	0.1	15.1	0.1	0.1	0.2	0.1	0.1	5.78
14.76	0.0	0.0	0.1	0.0	14.06	-0.7	0.1	0.8	0.1	0.7	0.1	0.7	0.1	5.79

Table 13. W49N 1665 MHz LCP Zeeman pairs

Vel (kms ⁻¹)	α off (mas)	σ (mas)	δ off (mas)	σ (mas)	Vel (kms ⁻¹)	α off (mas)	σ (mas)	δ off (mas)	σ (mas)	$\Delta\alpha$ (mas)	$\sigma(\alpha)$ (mas)	$\Delta\delta$ (mas)	$\sigma(\delta)$ (mas)	B mG
RCP 1665					LCP					RCP		LCP		
17.54	-51.2	0.1	745.2	0.1	17.56	-51.6	0.1	745.2	0.1	0.4	0.1	0.0	0.1	-0.03
10.90	585.7	0.1	435.6	0.1	14.62	585.4	0.1	433.8	0.1	0.3	0.1	1.8	0.1	-6.30
11.21	655.2	0.2	460.8	0.1	11.12	655.2	0.1	462.2	0.0	0.0	0.2	1.4	0.1	0.16
5.67	678.2	0.4	482.0	0.3	9.37	676.1	0.1	481.0	0.0	2.1	0.4	1.0	0.3	-6.27
7.79	657.0	0.0	454.7	0.0	7.78	657.0	0.1	454.7	0.1	0.0	0.1	0.0	0.1	0.01

Table 14. W49N 1667 MHz LCP Zeeman pairs

Vel (kms ⁻¹)	α off (mas)	σ (mas)	δ off (mas)	σ (mas)	Vel (kms ⁻¹)	α off (mas)	σ (mas)	δ off (mas)	σ (mas)	$\Delta\alpha$ (mas)	$\sigma(\alpha)$ (mas)	$\Delta\delta$ (mas)	$\sigma(\delta)$ (mas)	B mG
RCP	1667				LCP					RCP	LCP			
19.58	314.6	0.3	219.1	0.2	20.81	313.2	0.5	219.3	0.3	1.4	0.6	0.2	0.4	-3.46
20.71	7.0	1.2	85.5	0.9	20.57	11.4	0.3	94.7	0.3	4.4	1.2	9.2	0.9	0.41
18.84	-68.1	1.4	178.5	1.1	19.75	-70.2	0.1	183.6	0.1	2.1	1.4	5.1	1.1	-2.58
18.84	-68.1	1.4	178.5	1.1	19.00	-67.8	0.0	185.8	0.0	0.3	1.4	7.3	1.1	-0.45
17.63	251.3	1.4	188.2	0.7	18.80	252.1	0.4	185.9	0.3	0.8	1.5	2.3	0.8	-3.31
17.62	194.1	0.8	197.1	0.6	18.67	190.1	0.8	199.2	0.5	4.0	1.1	2.1	0.8	-2.98
17.71	363.2	0.5	993.6	0.3	18.61	351.3	1.2	988.2	0.9	11.9	1.3	5.4	0.9	-2.55
17.06	355.4	0.3	987.8	0.2	18.61	351.3	1.2	988.2	0.9	4.1	1.2	0.4	0.9	-4.37
17.34	127.4	0.4	-37.5	0.3	18.50	136.6	0.4	-44.2	0.3	9.2	0.6	6.7	0.4	-3.28
16.53	137.0	0.5	-36.7	0.3	18.50	136.6	0.4	-44.2	0.3	0.4	0.6	7.5	0.4	-5.57
16.50	314.1	0.3	851.4	0.2	18.05	314.0	0.5	851.0	0.3	0.1	0.6	0.4	0.4	-4.37
16.53	137.0	0.5	-36.7	0.3	17.76	137.3	0.2	-37.2	0.1	0.3	0.5	0.5	0.3	-3.49
14.30	-1423.8	0.1	36.0	0.1	17.86	-1423.1	0.7	34.6	0.4	0.7	0.7	1.4	0.4	-10.08
16.12	-67.3	0.6	406.1	0.4	17.20	-65.5	3.1	416.5	1.5	1.8	3.2	10.4	1.6	-3.05
18.53	-2243.2	0.5	2357.3	0.4	16.91	-2244.2	0.2	2358.7	0.2	1.0	0.5	1.4	0.4	4.59
15.21	-232.7	0.8	9.8	0.4	16.88	-233.9	0.5	10.2	0.3	1.2	0.9	0.4	0.5	-4.73
15.47	-86.6	0.1	128.9	0.1	16.76	-87.0	0.2	129.1	0.1	0.4	0.2	0.2	0.1	-3.67
15.35	368.3	1.1	528.1	0.8	16.58	373.0	0.8	525.2	0.5	4.7	1.4	2.9	0.9	-3.47
13.67	886.7	0.4	2191.3	0.3	15.81	886.0	0.3	2192.4	0.2	0.7	0.5	1.1	0.4	-6.05
13.22	954.0	0.3	443.9	0.2	14.77	952.2	0.4	443.5	0.2	1.8	0.5	0.4	0.3	-4.40
12.36	-336.9	0.2	325.9	0.2	14.02	-336.6	0.2	324.4	0.2	0.3	0.3	1.5	0.3	-4.67
11.60	920.2	0.3	767.5	0.2	12.17	913.3	1.8	765.7	0.9	6.9	1.8	1.8	0.9	-1.62
9.48	578.2	0.9	549.0	0.7	11.21	589.3	0.7	554.8	0.5	11.1	1.1	5.8	0.9	-4.88
10.39	844.2	0.8	689.0	0.6	10.51	837.0	1.0	703.1	1.1	7.2	1.3	14.1	1.3	-0.33
8.27	865.4	0.5	419.8	0.3	8.26	861.8	2.5	420.8	1.8	3.6	2.5	1.0	1.8	0.01
7.59	2207.9	1.0	1679.8	0.7	8.23	2208.2	1.9	1682.3	1.3	0.3	2.1	2.5	1.5	-1.82
6.39	2242.8	1.3	580.7	0.9	7.95	2246.8	1.1	578.9	0.6	4.0	1.7	1.8	1.1	-4.41
4.70	2908.4	1.2	3211.6	0.8	5.58	2909.2	1.6	3210.1	1.0	0.8	2.0	1.5	1.3	-2.46
4.72	3319.9	1.7	2602.4	1.3	5.55	3316.0	0.6	2606.8	0.4	3.9	1.8	4.4	1.4	-2.33
3.66	2759.0	0.2	3320.3	0.1	4.85	2761.6	0.1	3320.6	0.1	2.6	0.2	0.3	0.1	-3.36